PONTIFICIA UNIVERSIDAD CATOLICA DE CHILE
SCHOOL OF ENGINEERING

SPECIFIC FEATURES OF A CLOSED-END PIPE BLOWN BY A TURBULENT JET: AEROACOUSTICS OF THE PANPIPES

FELIPE IGNACIO MENESES DÍAZ

Thesis submitted to the Office of Research and Graduate Studies
in partial fulfillment of the requirements for the degree of
Master of Science in Engineering

Advisors:
MIGUEL RÍOS O.
PATRICIO DE LA CUADRA B.

Santiago de Chile, September of 2015

PONTIFICIA UNIVERSIDAD CATOLICA DE CHILE
SCHOOL OF ENGINEERING

SPECIFIC FEATURES OF A CLOSED-END PIPE BLOWN BY A TURBULENT JET: AEROACOUSTICS OF THE PANPIPES

FELIPE IGNACIO MENESES DÍAZ

Members of the Committee:
MIGUEL RÍOS O.
PATRICIO DE LA CUADRA B.
DOMINGO MERY Q.
SEBASTIÁN FINGERHUTH M.
ÁLVARO SOTO A.

Thesis submitted to the Office of Research and Graduate Studies
in partial fulfillment of the requirements for the degree of
Master of Science in Engineering

Santiago de Chile, September of 2015

Gracias a mi familia, mis amigos,

mis colegas y mis mentores.

ACKNOWLEDGEMENTS

I would like to give special thanks to my advisor Patricio de la Cuadra for his guidance and support, and for continuously sharing his experience and knowledge. I also wish to thank Benoit Fabre and Roman Auvray from the *Laboratoire d'acoustique musicale* (LAM) of the Jean le Rond d'Alembert Institute (UPMC) of the University of Paris VI, for their hospitality and their wise and helpful advice, and for a great teamwork experience. From the *Centro de Investigación de Tecnologías de Audio* (CITA) of the Institute of Music of the Pontificia Universidad Católica de Chile, I am especially grateful to Rodrigo Cádiz, Benjamín Carriquiry, and Paul Magron, for making this experience rich and for their kind help. I must also thank professor Miguel Ríos for facilitating the link to the Electrical Engineering department in this cross-disciplinary work.

TABLE OF CONTENTS

LIST OF FIGURES

LIST OF TABLES

ABSTRACT

Flute-like instruments with a stopped pipe were widely used in ancient cultures and continue to be used in many musical expressions throughout the globe. They offer great flexibility in the input control parameters, allowing for large excursions in the flux and geometrical configuration of the lips of the instrumentalist. For instance, the transverse offset of the jet axis relative to the labium can be shifted beyond the operational limits found in open-open pipes, and the total jet flux can be increased up to values that produce highly turbulent jets while remaining on the first oscillating regime. A replica of an Andean siku has been created to observe, using Schlieren flow visualization, the behavior of both the excitation and the resonator. Images and acoustic signals are captured from the experimental prototype while in resonant operation. Image processing algorithms are developed for extracting quantitative data from the oscillating jet, which is then used to fit the parameters of the proposed model. The internal acoustic pressure is also used for this purpose. The measurements of the jet wave propagation are in agreement with the literature, and a model for the prediction of the internal static pressure shows good agreement with the experimental results. Two phenomena are of particular interest: 1) the auto-direction of the jet towards the labium due to flow recirculation is measured for the first time, and 2) a shift in the overblowing threshold compared the case of open-open pipes is observed. Both effects help in extending the range of input control parameters that produce sound.

Keywords: physical models, flue instruments, stopped pipes, panpipes, siku, turbulent jets, jet visualization, jet detection.

RESUMEN

Instrumentos de la familia de las flautas de tipo extremo cerrado fueron usados extensivamente en culturas primitivas, y continúan siendo usados en varias expresiones musicales en el mundo. Estos instrumentos ofrecen gran flexibilidad en los parámetros de control, permitiendo amplias excursiones en las cantidades físicas del flujo y en la configuración geométrica del soplido y la embocadura del instrumento. Por ejemplo, el punto de incidencia del chorro contra el bisel puede ser variado más allá de los límites operativos de tubos abiertos, y la velocidad del flujo puede incrementarse hasta producir chorros altamente turbulentos sin cambios en el régimen de oscilación. Una replica de un tubo del siku fue construida para visualizar el comportamiento del chorro, usando la técnica de fotografía Schlieren. Imágenes y señales acústicas se capturan mientras el prototipo experimental se encuentra en resonancia. Posteriormente, se utilizan algoritmos de procesamiento de imágenes para extraer información cuantitativa de la oscilación del chorro, que luego se usa, junto con la presión interna del tubo, para ajustar los parámetros del modelo. Las mediciones de la propagación de onda en el chorro están en concordancia con la literatura, y un modelo para la presión estática interna pudo predecir las observaciones experimentales. Dos fenómenos son de especial interés: 1) por primera vez se ha medido la auto-dirección del chorro hacia el bisel debido al flujo recirculante, y 2) el umbral de cambio de modo de oscilación se desplaza hacia más altas velocidades de chorro, comparado con el caso de los tubos abiertos. Ambos efectos ayudan a extender el rango de parámetros de control que producen sonido.

Palabras Claves: modelos físicos, tubos cerrados, flauta de pan, zampoña, siku, chorros turbulentos, visualización de chorros, fotografía Schlieren, detección de chorros.

1. EXTENDED SUMMARY

1.1. Introduction

1.1.1. Physical Modeling of Musical Instruments

The physical principles governing the operation of musical instruments are a source of interest for researchers coming from several disciplines. Understanding the complicated phenomena underlying a violin string excited by a bow, or the oscillating stream of air issued from the lips of a flute player, require the simultaneous application of a great deal of knowledge. The motivation for such research may come from an instruments builder, a musician, or even an ethnomusicologist's perspective. All of this makes it for a rich area of study that brings together aspects of music, physics, mathematics, engineering, computer science, and more.

A successful physical description of a musical instrument can influence everything from the scope of the education of music players to the design of novel instruments. Perhaps, the most intuitive and common use of these models is the synthesis of sounds (the so called virtual instruments). Unlike other types of synthesis that focus on resembling the target instrument by analyzing its spectrum or timbre, or by manipulating audio samples, physical models are concerned with the nature of the sound source rather than the sound itself. Therefore, the resemblance between synthetic and real sounds relies on the precision of the description of the physical phenomenon. Moreover, the input parameters of these models are the same an instrumentalist can control, thus the manipulation of the output sound becomes very intuitive. Aspects such as the evolution of the timbre during the transient attack –which accounts for much of the identity of the sound– and the expressiveness of articulations, are a natural consequence of this approach (Verge, 1995). There are various other uses for physical models; for instance, they can help investigate the parameters that determine the playability of an instrument, or provide valuable insights on voice pathologies (Fabre, Gilbert, Hirshberg, & Pelorson, 2012).

1.1.2. The Panpipes

Flue instruments are wind instruments in which sound is produced by flow instability of a jet coupled to the acoustic standing wave in an adjacent resonator. The history of flue instruments dates back to tens of thousands of years ago (Fabre et al., 2012) and are believed to be the oldest tunable instruments (de la Cuadra, Smyth, Chafe, & Boaqiang, 2001). The raw materials for making a flute appear everywhere in nature, typically in the form of a hollow bone, a wood piece, a dried-up fruit shell, or a hollow cane, and producing a sound with such devices is a fairly simple matter. Resonators typically have a cylindrical shape, but conical and even spherical specimens have been found (de la Cuadra, 2005). On the other hand, the geometry of the excitation of the instrument can be fixed by the craftsman, like in the recorder or the organ pipes, or can be determined by the interaction between the lips of the player and the mouth of the instrument, as in the transverse flute or the panpipes.

The earliest arrangements of the flute were simple hole-less whistles; more elaborate arrangements like the panpipes appeared later on (Baines, 1967). The panpipes consists of a set of tubes of different lengths and radiuses attached together in a row or carved into one solid piece. Each tube is designed to produce a single note, and can be open or closed at the bottom. Musical aspects like the tuning scale depend on the specific culture in which the instrument is found. Although panpipes are present in many world cultures, the two main regions in which they appear are Malenesia and the Andean region of South America. Among the latter, the most widespread species and the main subject of study of this work, is the zampoña or siku.

Siku is the *quechua* name for most common Andean panpipe. It is also known as zampoña, a name appointed by the spaniards. The pipes of the siku are normally closed-end tubes made of bamboo shoots, split across two rows. One very common musical configuration is the duet, where two players alternate each note of the melody. Performances normally take place in open spaces and musicians dance while playing. These aspects have a direct impact in the playing technique used by the instrumentalists, and therefore in the

conditions of the excitation of the instrument. For instance, in order to produce the right timbre and loudness, the air jet is blown strongly and in short bursts, so that it becomes turbulent before reaching the edge of the pipe. The aesthetic emphasis in Andean music relies on the construction of a specific collective timbral texture, which varies depending on the specific local culture and the particular type of festivity (de Arce, 1998).

1.1.3. Why studying the siku?

Most flute-like instruments whose sound production mechanisms have been well studied have open-open resonators and are commonly blown with laminar jets (Fabre et al., 2012), such is the case of the transverse flute, the recorder, and the organ pipes. Acoustics and fluid dynamics in stopped pipes have received comparatively little attention. The traditional model for Western open-open pipes can be used as a basis to approach the study of stopped pipes, however, a specific analysis is required due the the differences in the fluid dynamics and the aeroacoustics of the excitation. In 2005, Fletcher (Fletcher, 2005) published a short but motivating article on the acoustics of the panpipes, in which he analyzes the geometry and tuning from both European and Andean panpipes. Other aspects like the blowing techniques of the instrumentalists, the intonation, and the basic aspects of the excitation were also presented.

On a similar line of work, some authors (Wright & Campbell, 1998; de Arce, 1998, 2002; Blanc, de la Cuadra, Fabre, Castillo, & Vergez, 2010) have shown interest in the intriguing sound and construction of a family of stopped pipes characterized by the use of complex resonators. The latter consists of two or more coaxial cylindrical tubes of different lengths and radiuses carved into one solid piece. The bottom end is stopped with a rubber cork, beeswax, or other similar material. Under a specific proportion of geometrical dimensions in the instrument, the right embouchure, and a very high speed blowing jet, an experienced player is able to produce a unique type of sound called *sonido rajado* (literally, torned sound). Normally found near the threshold between two oscillating modes, this sound is composed of a particular combination of harmonics that produce strong low frequency beatings. The use of complex resonators seem to have been rather common in all

the region of the Andes, specially in the pre-hispanic era. Contemporary use of these flutes continue to be present in some isolated local festivities of central Chile (de Arce, 1998), where the species called Flauta de Chinos can be found. Ethnomusicological studies of their ritual use and their orchestral disposition have been conducted by Pérez de Arce (de Arce, 1998). Wright and Campbell (Wright & Campbell, 1998) presented an analysis of the sound of the Chilean pifilca flutes, describing their tuning, and the power distribution of the harmonics in *sonido rajado*. Blanc et al. (Blanc et al., 2010) developed an acoustical model for the impedance in complex resonators, which was then contrasted with measurements and spectrum analysis of recorded sounds.

A description of the sound production mechanisms in complex resonators would require detailed flow measurements. This is a great challenge because the knowledge for the construction of an instrument with the adequate dimensions, and the production of this fluttering sound (*sonido rajado*) is very scarce. Taking these matters into a laboratory environment would be even more difficult. For the moment, studying the stopped pipes excited by turbulent jets is a first step in this direction.

1.1.4. Basic Aspects of the Sound Production Mechanisms of the Siku

The excitation in the siku is not fixed but can be varied by the musician. Figure 1.1 shows a diagram of the relevant parts of of the idealized geometry of the instrument. The jet emerges from the lips of the player with a direction x and travels towards a sharp edge located at the bore of the the pipe –the labium– through a small opening at the mouth of the instrument. The geometry can be represented by three degrees of freedom: 1) the distance along the x-axis from the flue exit O –the origin of the jet oscillations– up to the labium is W, 2) the orthogonal distance from the labium to the x-axis is the vertical misalignment y_{off}, and 3) the angle of inclination of the jet relative to the main axis of the pipe is α.

Sound production in flue instruments can be thought of as the coupling between an unstable jet and the resonant modes of a pipe. In resonant operation, the jet is surrounded by an acoustic field v_{ac} that perturbs the jet at its flow separation points ($x = 0, y = \pm h$). Because the jet is basically unstable, a wavy transverse perturbation $\eta'(x, t)$ is amplified

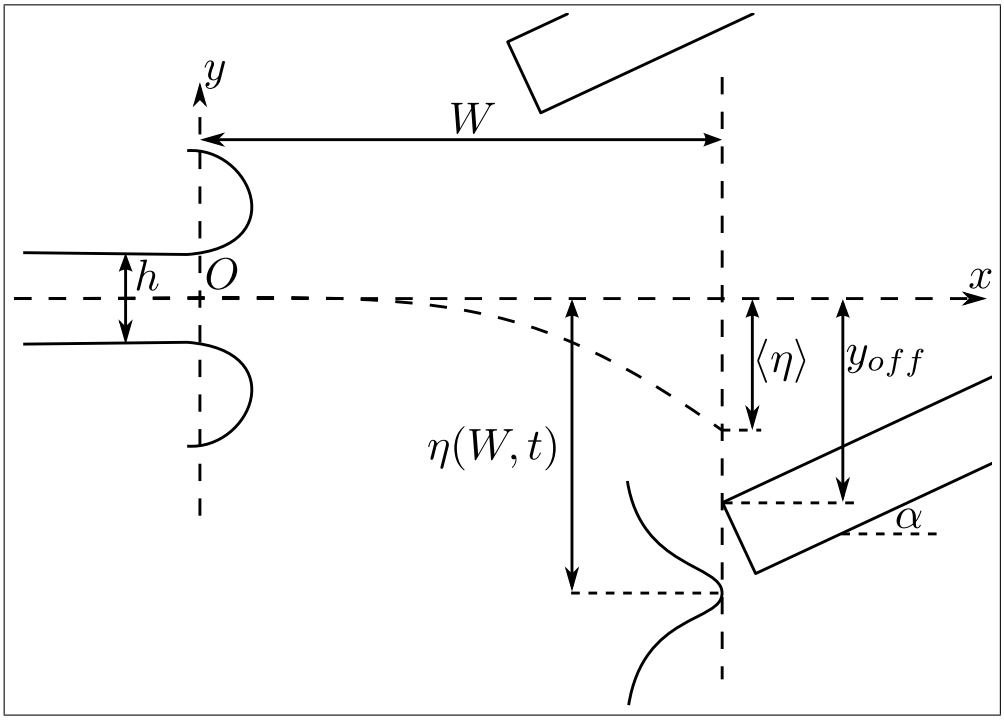

FIGURE 1.1. Schematic view of the excitation region of a flue instrument. The jet emerges from the "lips" at O, crosses the window of width W while being bent along the mean jet centerline $\langle\eta\rangle$ by flow recirculation. The x-direction is defined as the distance from the lip opening along the axis of the flue channel. The geometrical blowing conditions are characterized by the offset y_{off} between the jet axis and the labium, and the angle α between the jet axis and the pipe axis. During the auto-oscillation, the jet centerline $\eta(x,t)$ oscillates around its mean deviation $\langle\eta\rangle(x)$.

while convected downstream. At the labium the jet is split inwards and outwards, and the subsequent out of phase flow injection is usually described as a pressure source – a force driving the air column inside the pipe. The resonator acts as a filter, amplifying the source near its resonant frequencies and creating the acoustic field that closes the feedback loop.

Mass conservation in a closed-end tube requires that the mean part of the jet flowing into the pipe must leave via the same place it entered: the blowing end. This results in a static component of the pressure gradient along the pipe and a subsequent steady component of the flow directed cross-stream to the jet. The jet flowing towards the labium crosses

this area where it is deflected by the interaction with the crossflow. Therefore, the total vertical displacement $\eta(x,t)$ is the sum of the oscillatory component of the wavy perturbation $\eta'(x,t)$ and the static deflection due to the crossflow $\langle\eta\rangle(x)$.

The Reynolds number ($Re = u_0 h/\nu$, where u_0 is the jet central velocity and ν the fluid viscosity) describes the structure of the jet. Re varies from a couple of hundreds in instruments like the recorder, up to near 10000 in the transverse flute (de la Cuadra, 2005). As Re increases beyond 2500–3000 turbulence appears in the jet, which is then filtered by the resonator, adding a characteristic color of breathy wideband noise. This accounts for much of the identity of the sound in most flue instruments (Verge, 1995), and it is even more relevant in the case of the siku (Fletcher, 2005). Moreover, turbulence induces a rapid spreading and slowing of the jet, which affects the velocity of convection of the acoustic perturbations (Thwaites & Fletcher, 1980).

1.1.5. Thesis Overview

The main purpose of this work is to measure the joint effect that the stopped pipe and the turbulent excitation have on the aeroacoustical behavior of the instrument. Experimental data, such as flow visualization images and pressure traces, is gathered from a laboratory replica of a siku. The data is then processed with specific algorithms, and used to fit fluid dynamic and acoustic models of the instrument.

The experiments were conducted at the flow visualization laboratory of the LAM (*Laboratoire d'acoustique musicale*), a center of the institute *Jean le Rond d'Alembert* of the University of Paris VI. The image processing algorithms developed for this work were presented in the article *Aeroacoustic of the Panpipes* for the 21st International Congress on Acoustics held on Montreal between the 2-7 of June 2013.

The document is structured as follows: Chapter 1 contains an extended summary of the work including hypotheses, objectives, a state-of-art review, methodologies, main results, and conclusions. Chapter 2 is the main body of work, constituted of an article submitted to the *Journal of the Acoustical Society of America*, where a physical model of the siku is

presented, experiments and data processing algorithms are described, and the main results of the investigation are laid out. Finally, chapters A, B, and C of the Appendix describe specific aspects of the experimental procedure and the image processing algorithms.

1.2. Hypotheses

While turbulent jets and some aspects of stopped pipes have been studied independently, there is no evidence as to how their combination would modify the behavior of a real instrument. For instance, stopped pipes seem to tolerate a wider range of jet velocities while remaining in the first oscillating mode. This relaxation of the input control could help extending the range of possible configurations of the excitation, modifying important aspects of the sound, such as the power distribution of harmonics and the ratio of harmonics to noise. Therefore, the variation of the timbre could be more accessible to novice players in stopped pipes. Furthermore, it has been observed that the joint effect of turbulence and the steady crossflow may alter oscillations in the jet (Nolle, 1998; de la Cuadra, Vergez, & Fabre, 2007) and its velocity profile. This could have an effect on the delay of convection of the perturbations from the flue exit to the labium, an important parameter for the auto-oscillation balance.

Fletcher (Fletcher, 2005) proposed, on theoretical grounds, that the interaction of the blowing jet and the recirculating flow inside the pipe yields a hydrodynamic balance that helps directing the jet's centerline near to a set point: the labium. His analysis suggests that the direction of the jet is fixed by the aerodynamical balance in the stopped pipe, rather than by the configuration of the lips. This would imply that the player does not need to aim sharply at the labium in order to produce sound. Such observation has not been supported with data and there are no available models that can predict the phenomenon.

From the experimental point of view, it has been shown (Yoshikawa, 1998; de la Cuadra et al., 2007) that image processing techniques applied on Schlieren images of jets can be used to extract quantitative information of the flow instability. However, these approaches focused on laminar jets and made experimental simplifications that altered the

natural conditions of a real sounding instrument. It is expected that the technical difficulties of graphic and audio noise induced by turbulence, can be overcome by means of the adequate filtering techniques, thus making it possible to obtain a numerical representation of the instability of the turbulent jet in a sounding instrument.

1.3. Objectives

This investigation aims to get a general understanding of the effect that the closed-end and the turbulent excitation in the siku have on the physical quantities described by the traditional flute model. The main objectives are:

- Develop a model for the flow balance inside the stopped-pipe resonator, with special focus on the static pressure gradient and its subsequent steady outflow.
- Measure how the simultaneous effect of the stopped pipe and the turbulent excitation affect the main parameters of the jet instability: the amplification and convection velocity of the wavy perturbation
- Evidence, with support of quantitative information, the auto-direction effect of the jet in stopped-pipes proposed by Fletcher (Fletcher, 2005).
- Investigate how the playability of the instrument, in relation with the input control parameters, is modified by the characteristics of fluid dynamics in the stopped pipe.
- Study the main characteristics of the radiated sound, relating them to the control parameters of the excitation: the jet velocity and the geometry of the mouth of the player.
- Design an experimental setup that allows to obtain jet images and pressure traces from a stopped-pipe in resonant operation. The data should be suited for a detailed analysis using image and audio processing algorithms. One of the objectives is to obtain a quantitative representation of the instability of the turbulent jet.

1.4. Literary Review

1.4.1. Physical Models of Flue Instruments

The physics governing the operation of flue instruments has called the attention of scientists for centuries. Early figures such as Daniel Bernoulli were concerned with fundamental aspects, like the relation between the geometrical dimensions of the resonator and the frequency of the tone produced (de la Cuadra, 2005). With the studies of Helmholtz (Helmholtz, 1885) and Rayleigh (Rayleigh, 1894) came the first formal descriptions of the mechanisms of sound production in flue instruments. The authors described the nature of the acoustical source as an oscillating force term proportional to the blowing pressure, acting near the edge of the labium (Verge, 1995). Rayleigh also proposed a simplified model for the oscillations of the jet, based on the linear instability analysis of an infinitely extended frictionless flow (Fabre & Hirschberg, 2012), which is still widely used as a basis for more elaborated models.

In the early sixties Powell (Powell, 1961) developed a quantitative model for the edgetone, a configuration where the jet impinges on an edge on free-field conditions, that is, without a resonator. He conceived the system as a feedback loop made of separate elements: a filter, an amplifier, and two delays, whose interaction was assumed to be punctual. The idea was then extended to the case of a functioning flue instrument by Cremer and Ising (Cremer & Ising, 1967-68). This approach, called lumped elements, allowed for an isolated analysis of the resonator, the jet hydrodynamics, and the aeroacoustical sources (Auvray, Fabre, & Lagree, 2012). Even if such a separation was hard to justify, it made possible the development of sound synthesis models that became extremely popular (Fabre & Hirschberg, 2012). Between the decades of the sixties and the nineties, several authors took up on this framework ((Coltman, 1967, 1968; Elder, 1973; Fletcher, 1976; Holger, Wilson, & Beavers, 1977; Verge et al., 1994; Verge, 1995; Verge, Hirschberg, & R.Caussé, 1997), among others). In an article published on the year 2000, Fabre and Hirschberg (Fabre & Hirschberg, 2012) reviewed the historical development of lumped

models, comparing them to the more rigorous integral models. Because of the mathematical complexity of the hydrodynamical problem, the validity of an integral analysis seems limited to idealized geometries and unrealistic flow conditions. Since lumped models are non-linear fits of experimental data, they can predict a complicated phenomenon without necessarily providing an explanation to it. In Fabre's opinion, experimentation is and will continue to be the main source of new fundamental results.

1.4.2. Quantitative Analysis using Jet Visualization

As stated in section 1.4.1, experimentation is the main source for generating new results in flute modeling. Various techniques are used to obtain quantitative data from the flow in flue instruments, for instance: pressure sensors are used for measuring static and acoustic signals, and hot-wire aneomometers serve for characterizing the velocity profile of the blowing jet. The introduction of these measuring devices often collides with the production of sound, altering the natural conditions of the instrument –that is, if sound is produced at all. Jet visualization is a less invasive technique that requires an expensive experimental setup and post process of the data. Jet visualization has been used as a complementary source of information (Verge et al., 1994; Verge, 1995; B. Fabre and & Wijnands, 1996), aimed mainly to help understanding some behavioral aspects of the flow, such as the formation of vortical structures, the transition from laminar to turbulent regimes, the formation of the jet, and the transient attack.

In order to make air jets visible, smoke or vapor can be used as a blowing source, which yields a rough representation of the shape of the jet. A more elaborate alternative is Schlieren photography, which allows to visualize mass gradients within a fluid. Its implementation requires a sophisticated setup that involves an array of lenses, a synchronized illumination system, and a fluid source of different mass density than air (normally CO_2). Some authors have used this imaging technique on free jets (de la Cuadra, 2005; de la Cuadra et al., 2007) as well as on laboratory replicas of flue instruments (Yoshikawa, 1998).

Flow images require an elaborated post process in order to obtain quantitative information from them, and few authors have developed this necessary tools. Yoshikawa (Yoshikawa, 1998) presented an envelop-based method to estimate the growth factor of the jet wave in an organ pipe. Using a smoked jet and a high speed video camera, images of different instantaneous phases are superposed, yielding an estimation of the evolution of the wave crest. Parameters of the jet oscillations are estimated using information of the crests, needless of an actual representation of the wave. A more thorough image processing method was proposed in (de la Cuadra et al., 2007), using Schlieren images of an acoustically perturbed jet (the edge and the pipe are replaced by loudspeakers). Two image processing alternatives were developed to detect the median line of the jet, which was then used to estimate the parameters of the wavy perturbation. The first was an inter-image approach based on morphological segmentation of one image at a time. The second was an inter-image approach, that used the cross-correlation between consecutive phase-adjacent images to measure the relative displacement of the jet. Both methods showed promising results with specific performance advantages: while the detection using the cross-correlation was more sensitive to image noise, the morphological segmentation had to be re-calibrated for each set of images.

1.5. Methodology

1.5.1. Overview of the Procedure

As stated in section 1.4.1, sound production in flute-like instruments is commonly modeled using lumped elements. This approach is a combination of theoretical formulations and curve fitting of experimental data. Therefore, experiments are designed to allow for the measurement of flow and acoustic quantities, that serve to adjust the parameters of the models.

On real instruments, a series of geometrical and hydrodynamical conditions need to be met in order to generate an optimal sound. Pressure sensors and other captors that interfere in the way of the jet could damp the oscillations and alter the overall acoustical behavior of the instrument. For this reason, some authors have opted for exciting free, unconfined jets,

with an external acoustic source such as a loaudspeaker (de la Cuadra et al., 2007; Nolle, 1998; Thwaites & Fletcher, 1980, 1982). This is a valid approach to study the instabilities of the jet and the evolution of the velocity profile. However, it disregards important aspects such as the jet-labium interaction and the flow balance in the resonator.

In the present work, the aim is to measure the simultaneous effect of the turbulent jet and the recirculating crossflow induced by the stopped pipe. Therefore, it is of interest to bring this matters into a laboratory environment under conditions as realistic as possible. Flow visualization demands some modifications to the resonator, such as the construction of a transparent window of observation, but it is otherwise harmless to the experimental conditions. It requires, however, a complex algorithmic development to extract information that is hidden within the images.

Fluid dynamic and acoustic models are developed for the purpose of interpreting the data gathered from experiments on a laboratory replica of a siku. Possible modifications of the traditional flute model are explored, so as to include the implications of turbulent jets and jets in crossflow. An experimental procedure for the measurement of some hydrodynamic properties of an air jet in a real instrument configuration is presented. A Schlieren visualization scheme is implemented on a laboratory replica of an Andean siku that is blown with a turbulent jet. An algorithmic routine is developed in order to handle large amounts of audio and image data, to semi-automatically transform the raw images into a useful numerical representation of the jet oscillations. Finally, the parameters of the models are fitted using the experimental results.

1.5.2. Laboratory Experiments

Experiments are designed with the aim of obtaining quantitative flow measurements from Schlieren images of the jet. Both, the instrument and the player are replaced with laboratory prototypes that resemble the characteristics of the real scenario. The largest design restriction is the clearance of a region of interest near the labium of the instrument that allows for flow visualization even within the pipe. Acoustic signals inside and outside the

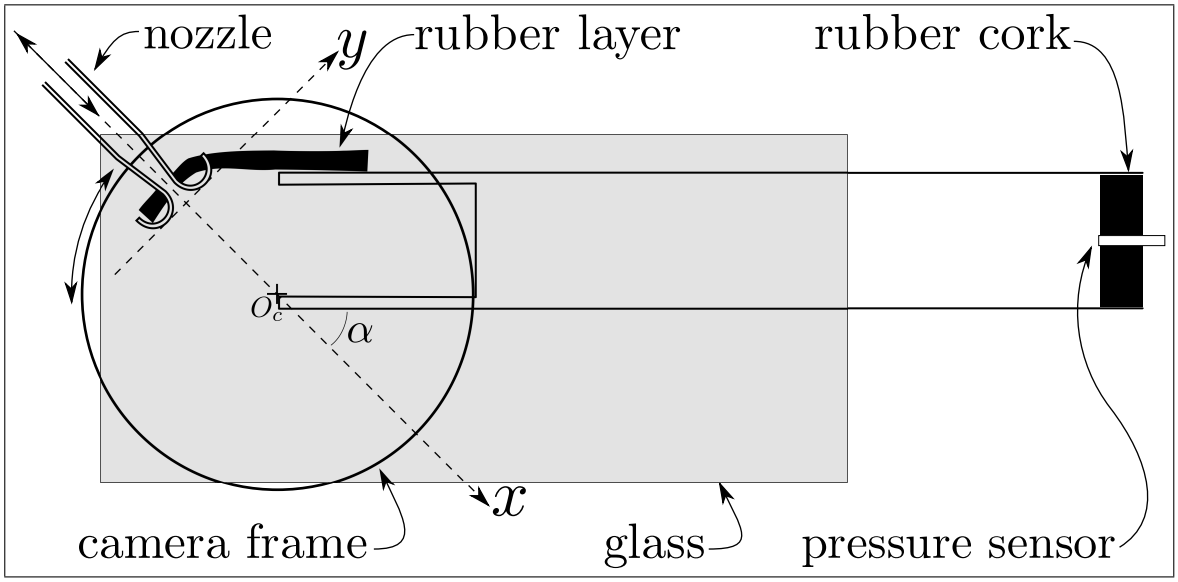

FIGURE 1.2. Sketch of the experimental setup: Pipe and nozzle as seen by the camera through the glasses. The nozzle can rotate around the center O_c and can be translated along the x axis.

instrument are used to synchronize jet oscillations within the images, and also to analyze the harmonic composition of the sound of the instrument.

The instrument, a laboratory replica of a siku, was built with the modifications necessary to allow for jet visualization and pressure measurement at the closed-end (see Figure 1.2). The pipe is an aluminum tube of square cross section. The dimensions of the pipe were chosen using the power law traditionally found in panpipes (Fletcher, 2005): $D = 1.32L^{0.43}$, where D is the equivalent diameter of a circle of the same surface as the square cross-section pipe, and L the pipe length. This provides a fundamental frequency of approximately 690 Hz. In the region near the open end, two opposite walls were cut off and replaced with two larger pieces of transparent glass so as to clear out a visualization area.

The round edges of the flue exit attempt to resemble the lips of a human player. An additional rubber piece is used to seal the gap that is normally filled by the the lower lip of the instrumentalist. The pipe and the nozzle are mounted on a system that allows for the adjustment of the jet-pipe angle α; while the pipe remains fix in its position, the flue exit is

allowed to rotate orthogonal to the perimeter of a circle of radius W. This last parameters is adjusted heuristically to produce the adequate sound. A mass flow regulator is used to indirectly control the Reynolds number.

A carbon dioxide jet is blown into the pipe to provide a mass gradient with the surrounding air, a necessary condition for Schlieren visualization. The experimental arrangement permits to adjust the jet-pipe angle α, the jet-labium misalignment y_{off} and the Reynolds number $Re = u_0 h/\nu$ –varied through the jet velocity u_0 –, for a slit of height h and a fluid of viscosity ν.

Each experiment consists in the acquisition of N=368 images at a rate of 8 Hz ($\sim$ 46 sec) under steady conditions of the control parameters. Turbulent jets on the range $Re \simeq 3000 - 6500$ are investigated, for angles α between 24° and 68°, and for two jet offset configurations y_{off}=0 mm and y_{off}=3 mm. In all cases the instrument is able to produce sound.

Specific details of setup and the equipment used are presented in appendix A.

1.5.3. Image Processing Algorithms

The images present several challenges from the viewpoint of their analysis. For instance, one of the control parameters is the jet-pipe angle, which means that the geometrical configuration (the position of the pipe within the frame) changes constantly. Thus, a special processing is needed in order to define a homogeneous window of observation. Furthermore, the video frame rate (8 Hz) is not synchronized with the oscillation frequency of the jet ($\sim$ 690 Hz), so that no direct representation of motion can be deduced from the images. Finally, small vortical structures of the turbulent jet difficult the detection of the centerline.

The oscillating pressure at the closed end of the pipe p' is used as a reference for the harmonic motion of the jet. On the other hand, the camera is synchronized to a square-pulses signal, which is processed together with p' to yield a phase and amplitude label for

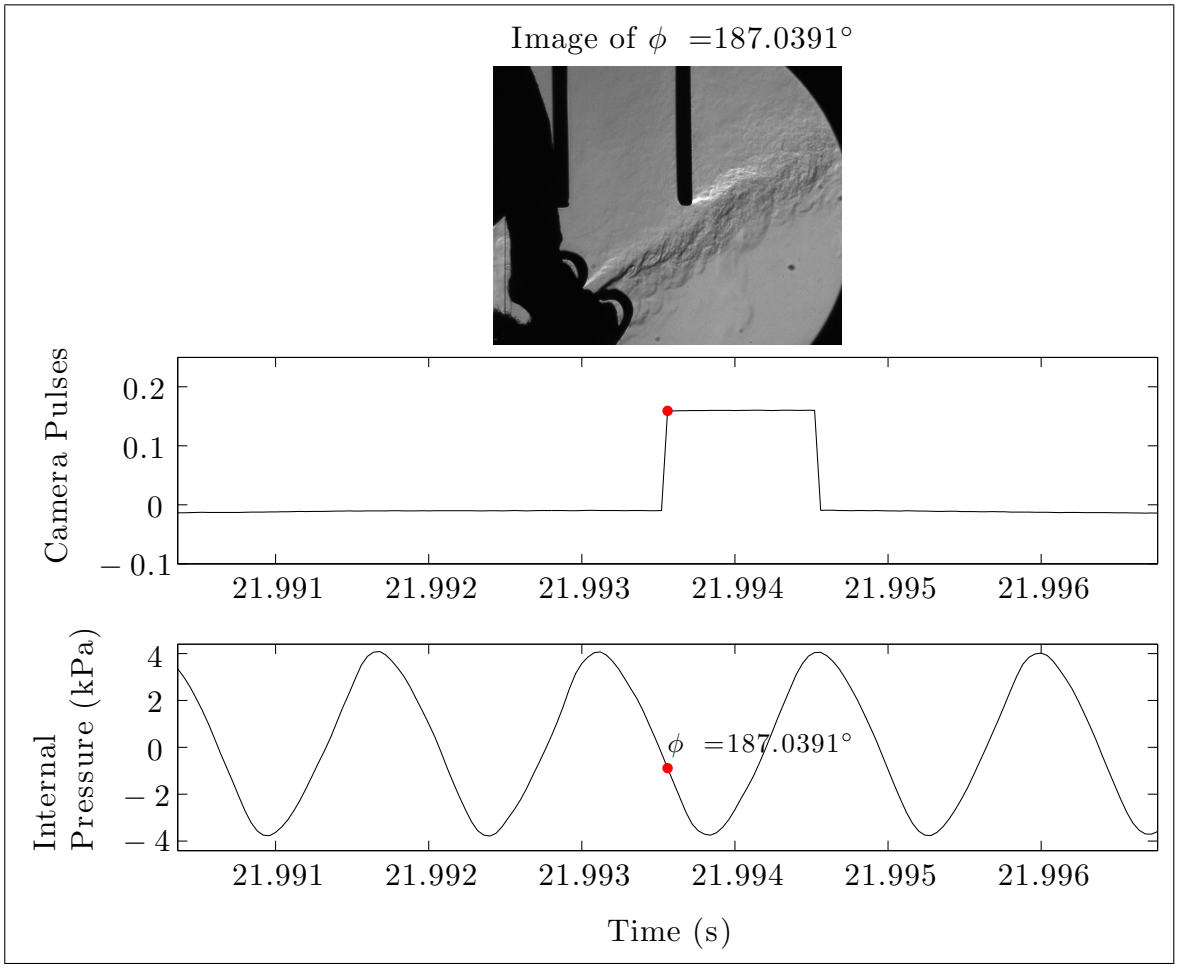

FIGURE 1.3. Scheme of the image phase-labeling method: The jet in the image has an instantaneous phase of ϕ and is linked to a pulse of the camera top signal (center graph). The sample at the rising edge of the strobe (red dot) is used to determine the instantaneous phase of the pressure signal inside the pipe ϕ=187.0391° (lower graph), which corresponds to the phase label of the image.

each image. Figure 1.3 explains this process. Therefore, a complete cycle of oscillation can be reconstructed by sorting images according to their instantaneous phase.

The original size and orientation of the images is cropped and rotated, using the nozzle structure as a reference in an image registration algorithm (Maes, Collingnon, Vandermeulen, & G. Marcha, 1997) (see Appendix B). Then, as a way of reducing the effects of turbulence, a method for smoothing images that uses information from several phase-adjacent ones is proposed. These are called "aggregated" images to differentiate them from

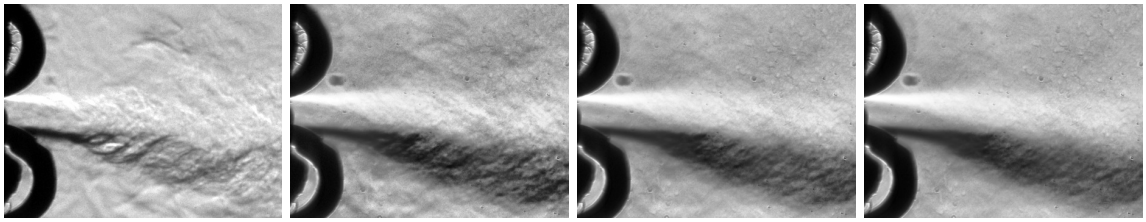

FIGURE 1.4. Image aggregation process for three different spread parameters ζ and $(Re, \alpha) = (5700, 46°)$. ϕ corresponds to the instantaneous phase of the acoustic signal at the moment of the capture of the single-shot image, and φ is the central phase of the image aggregation algorithm.

the original "single-shot" ones. Finally, a simulated period of oscillation is created by uniformly selecting 32 images in the range $[0 - 2\pi]$. This is done for both single-shot and aggregated images.

Figure 1.4 shows aggregated images for different values of the spread parameter ζ, which accounts for the smoothing of the aggregation process (see Appendix 2.4.1. for a detailed explanation). In this representation, unsynchronized patterns (turbulent small-scale vortical structures) are deconstructed, thus favoring the analysis of the centerline.

A modified version of the cross-correlation algorithm proposed in (de la Cuadra et al., 2007) was used to detect the centerline of the jet $\eta(x, t)$. Aggregated images are used for this purpose. A harmonic analysis of $\eta(x, t)$ is performed in order to obtain the mean deflection $\langle\eta\rangle$, the amplitude $|\eta'|$, and the phase $\phi_{\eta'}$ of the jet wave. Curve fitting is then used to extract the mean deflection coefficient δ and the amplification factor of the jet wave α_i. The length l_e is obtained by running the centerline detection algorithms on single-shot images, and measuring the point where the detection is no longer possible due to turbulent noise. This length (l_e) is considered the point where the shear layers collapse and turbulence reaches the center of the jet, affecting its spreading and velocity profile.

The overall structure of the program consist in: codifying and preparing the raw data, synchronizing the analog signals with the images, processing the images, detecting and

analyzing the jet, and finally fitting the models to the extracted information. A schematic representation of the routine is presented in figure 1.5.

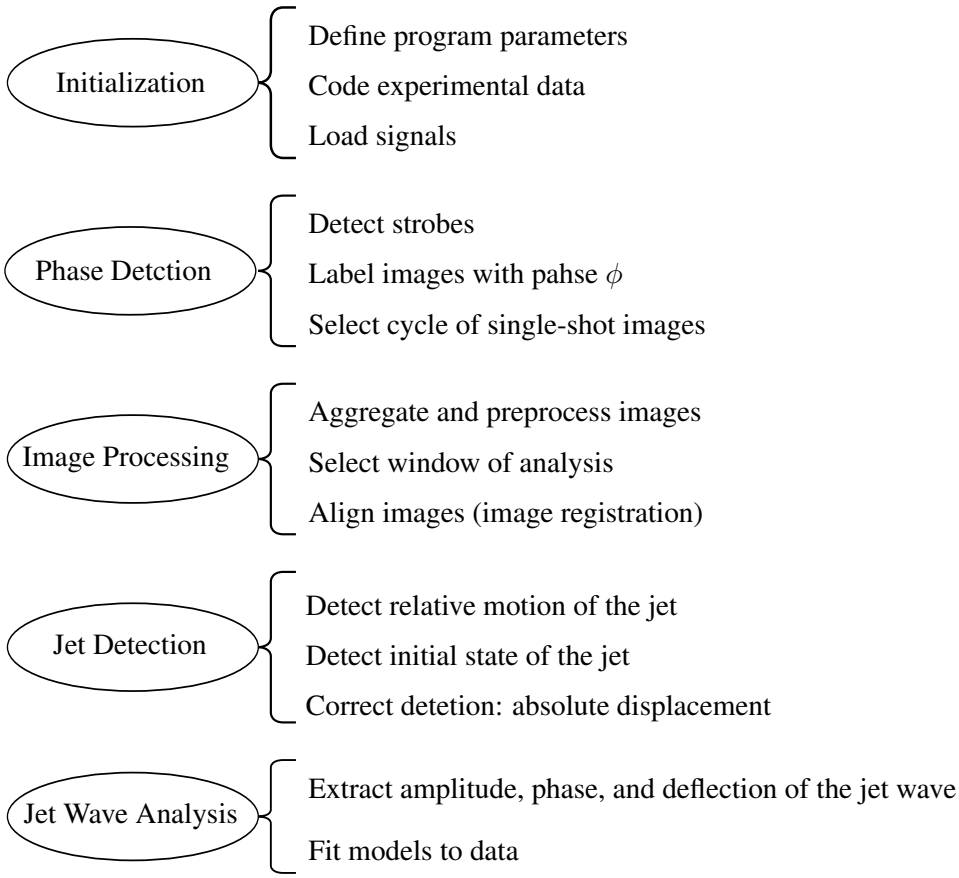

FIGURE 1.5. Schematic division of the program devised for extracting hydrodynamic information from the images.

1.6. Results

The results are laid out in two sections: first, the performance of the jet detection algorithms is tested using synthetic images, and second, the experimentally-fitted physical models are evaluated and compared to those found in the literature.

1.6.1. Jet Detection Algorithms

The performance of the algorithmic routine described in section 1.5.3 is tested using an artificial set of images of a computer-synthetized oscillating jet (see Appendix C for an extended analysis). Synthetic images are created using similar quantities to those observed in the real images. For instance, the perturbation of the jet is modeled using the linear stability analysis valid for laminar jets (de la Cuadra, 2005):

$$\eta'(x,t) = e^{\alpha_i x}\eta_0(t - x/c_p), \tag{1.1}$$

where α_i is the amplification coefficient, c_p the velocity of convection, η_0 the initial displacement, and ω the angular frequency of oscillation. The initial width of the jet is set at $h = 0.7$ mm and the shear layers spread with an angle of 22°, yielding a final jet width similar to the experimental case. Turbulence is simulated using consecutive rounds of Gaussian noise of mean 0 and variance 50%. A level of Noise=2 means applying Gaussian noise two consecutive times, and so on.

The detection algorithms are now applied to each set of synthetic images. The resulting jet wave is used to the deduce the parameters of Equation 1.1, without any knowledge of the parameters that were used to generate the wave. This is done with curve fitting. Finally, a comparison can be done between generated and detected parameters, measuring the effect that the exogenous processes of noise and aggregation have on the performance of the detection. Table 1.1 summarizes this process.

Results show that with single-shot images is possible to reconstruct the jet wave with high precision if the images have low levels of noise. For Noise=3 the performance drops dramatically and for Noise=4 the jet could not be detected. On the other hand, aggregated images are less sensitive to noise, but tend to underestimate the growth of the jet wave (α_i) because large oscillations are averaged with smaller ones. However, the values of α_i obtained with these images are consistent throughout levels Noise$\leq$3, and have a drop of $\sim$7% for Noise=4.

TABLE 1.1. Estimated jet wave parameters for single-shot and aggregated images under different conditions of noise. Synthetic images are generated with parameters are $\eta_0 = 0.05$, $\alpha_i = 0.33$, and $c_p = 10$ m/s.

	Single shot			Aggregated		
Parameter	η_0	α_i	c_p	η_0	α_i	c_p
Generated	0.05	0.33	10	0.05	0.33	10
Detected						
Noise=0	0.0479	0.3323	9.9995	0.0521	0.3190	10.024
Noise=1	0.0471	0.3338	9.9812	0.0532	0.3178	10.034
Noise=2	0.0529	0.3165	9.9268	0.0551	0.3132	9.988
Noise=3	0.0638	0.2423	9.9481	0.0510	0.3153	9.965
Noise=4	–	–	–	0.0638	0.2985	9.881

The image aggregation method is also tested using synthetic images, for different conditions of background noise. Values of the spread parameter $\zeta \geq 8°$ showed to have destructive effects for large amplitudes of oscillation, because the positive vertical displacement tends to be averaged out with the negative one. On the other hand, larger values of ζ are more effective at deconstructing non-syncrhonized structures such as the background noise. Therefore, a trade-off between these two performance characteristics needs to be found for a specific set of images. In our experiments ζ is set to 8.4°.

The detection of the centerline on a real set of images is illustrated in figure 1.6. On aggregated images, the detection shows a reliable performance on most of the jet path. Towards the end of the region of interest (x/h >8) the centerline can no longer be detected with precision. On single-shot images, the detection is only valid within a small region near the flue exit, that is, just before the jet-core collapses due to turbulent mixing. This particular feature is utilized to estimate the distance of establishment of the self-similar velocity profile l_e (see 2.2.2.2).

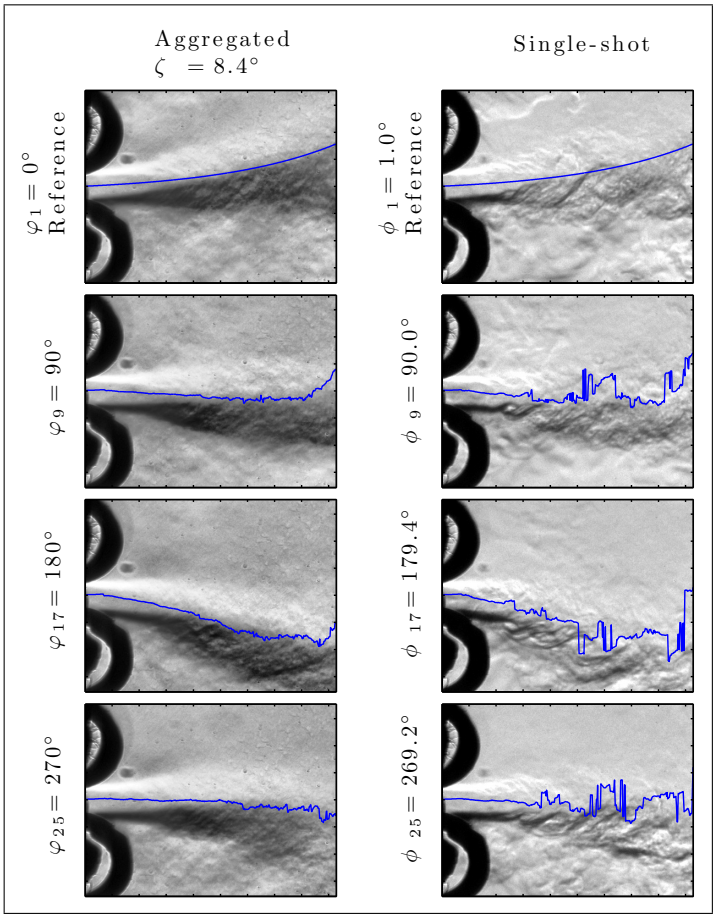

FIGURE 1.6. Detection of the centerline $\eta(x,t)$ (blue line) in single-shot and aggregated images for $(Re, \alpha) = (5700, 46°)$ for a set of 32 images of a complete cycle of oscillation of the jet wave. φ_i and ϕ_j correspond to the ith and jth image of the aggregated and single-shot sets, respectively.

1.6.2. The Model

Following the traditional taxonomy of lumped elements, the evaluation of the model is divided into the aspects that concern the effects of the stopped-end resonator, and the effects of the turbulent excitation.

1.6.2.1. The Resonator

A model of the pressure difference Δp at the closed end was developed. The predictions of the model have the same order of magnitude and tendency than the experimental

results, but show an overestimation of the pressure decay for values of α>45, and do not predict the observed dependency with Re.

1.6.2.2. The Excitation

The effects on the excitation of the steady recirculating crossflow in a stopped pipe have been experimentally measured for the first time. As it was suggested by Fletcher (Fletcher, 2005), the final position of the jet's centerline is almost entirely fixed by the crossflow rather than the geometrical configuration. When the x-axis is misaligned with respect to the labium ($y_{\text{off}} \neq 0$), the steady deflection helps auto-directing the jet to a point slightly above the labium, thus maintaining the self sustained oscillations. A simple model for the steady deflection with an exponential dependency on the x distance is proposed. Results are in good agreement with values found in the literature for similar configurations, showing no dependency on any of the experimental parameters.

For the values of Re tested (3000-6500) the shear layers are already turbulent at the flue exit, with a laminar core that collapses at a distance from the origin $x = l_e$. The jet central velocity u_0 is assumed to be constant within the laminar core region ($x < l_e$), and then decrease according to $u_0 \propto x^{\frac{1}{2}}$ (see Eq. (2.9)). Furthermore, the convection delay of the perturbations, an important parameter in the auto-oscillation process, is highly dependent on u_0. The detected values of l_e have a consistent dependency on the Reynolds number, which could allow for the development of a prediction model.

The instability of the jet is characterized using two parameters: the amplification factor $\alpha_i = \beta/h$, used to predict the amplitude of the oscillations that generate the sound, and the propagation velocity $c_p = \gamma u_0$, that accounts for the delay of convection and ultimately for the sounding fundamental frequency. The harmonic analysis performed on the detected centerline yields the wave amplitude $|\eta|$ and the phase ϕ_η, which are used to fit α_i and c_p, respectively. Our study shows –and other studies confirm– that α_i does not depend on the Reynolds number. However, a dependency on the geometrical configuration was observed: for $y_{\text{off}} > 0$, the amplification factor is larger and also shows a relation to the jet-pipe angle α. The convection velocity c_p could not be measured accurately because it depends

on the derivative of a noisy vector: the phase ϕ_η: $c_p = \omega(d\phi_{\eta'}/dx)^{-1}$. However, a shift of tendency in ϕ_η that coincided with the estimated establishment length l_e was observed, which indicates that both quantities are correlated.

The overblowing threshold is commonly described in terms of the Strouhal number $St_w = fW/u_0$. Experimental observations in open-open pipes show that, for values of Re as high as 5200, St_w is expected to reach the overblowing threshold of 0.07. In the case of the siku, the lowest registered value of St_w was 0.1, for Re as high as 5800. The observations on the evolution of the central velocity can partially explain this phenomenon: as the jet velocity u_0 is raised, the effects of turbulence are triggered closer to the flue (l_e), which causes a greater slowing ($u_0 \sim x^{\frac{1}{2}}$). This in turn increases the delay of convection of the perturbations ($\tau \sim 1/f$). Therefore, the effect of an increase in Re on the final delay, is counterbalanced with a decrease in l_e, which extends the admissible jet velocities within the first register of the instrument.

1.7. Discussion and Conclusions

Some fundamental aspects of the hydrodynamics of stopped end pipes have been discussed analytically and observed in a controlled experiment. The musician has direct control over several parameters, such as the jet-labium offset y_{off}, the central velocity of the jet u_0, and the jet-pipe angle α. Changes in any of these three parameters have an incidence on the hydrodynamic behavior and thereby on the acoustic behavior. We have observed that a wide range of these parameters produce sound.

The most remarkable observation has to do with the jet-labium offset: the player does not need to aim the jet directly at the labium in order to produce stable oscillation. When the jet is directed to the labium, the mean deflection of the jet centerline due to air recirculation within the pipe seems to act only on the first half of the jet path. The resulting deflection at the labium represents a small deviation as compared with the open-open pipe case. When the jet is not directed at the labium but towards the center of the pipe inlet, the mean deflection makes the jet bend back towards the labium, providing a total deflection that

is, in average, three times higher than that of the former case. This observation supports Fletcher's statement (Fletcher, 2005): the jet gets auto-directed towards the labium due to its interaction with the steady outflow. The mean jet centerline position is almost entirely fixed by the aerodynamic balance rather than by the lip's configuration, as it would be in the case of an open-open pipe.

Stopped pipes also tolerate a wider range of jet velocities in the first oscillating regime, compared to open-open pipes. In the former case, the overblowing threshold is shifted to a higher jet velocity, partly due to the characteristic slowing of the turbulent jet, and also due to the concurrence of the second pipe mode near the third harmonic of the fundamental, instead of the second harmonic, as in an open-open pipe. Moreover, as the initial velocity u_0 is raised, turbulent mixing on the jet is triggered closer to the flue and thus the characteristic slowing of turbulence has a greater impact. As a consequence, a higher velocity is necessary to achieve the overblowing, which has the musical advantage of allowing a larger dynamic range within the first register. Along with the hydrodynamical consideration, increasing the jet velocity also affects the oscillating frequency, which, in the present experiment, can be increased about one quarter tone.

Another striking point is the wide range of angles at which the pipe is able to produce stable oscillations. No specific trend on the jet behavior has been identified, however, both the oscillating frequency and the acoustic power showed a correlation with the angle.

From the standpoint of the musician, this study concludes that the production of a tone in stopped-pipes is a simple task compared to the case of an open-open flue instrument, mainly because misalignments of the jet are corrected by the hydrodynamic configuration. Furthermore, the mechanisms of variations of the timbre dependent on the jet velocity, are of easy access for both novice and experienced players. Although these variations are performed at the expense of the intonation, the latter is a far less relevant aspect in the musical tradition of the Andes. These reasons might partly explain why stopped pipes were the most common type of resonator found in ancient civilizations of the region, and also how that influence helped shaping the aesthetics of their music.

1.8. Future Work

The physical modeling synthesis of a stopped pipe blown by a turbulent jet seems within reach by adding few modifications to the existing flute model. One main feature of such instruments is the broadband noise filtered by the resonator, which could be handled as proposed by Verge *et al.*(Verge, Hirschberg, & R.Caussé, 1997). Furthermore, modifications to the spreading and slowing of the jet are introduced by the trigger of turbulence, increasing the total delay of the model, and shifting the overblowing thresholds. An adjustable parameter based on the establishment length of turbulence l_e can be introduced to account for the slowing. The mean jet deviation and the final transverse offset should also be considered; these are dependent on whether the jet is originally directed at the labium or towards the inside of the bore. In the latter case, the growth rate of the jet instability is increased.

Considering the range of Re that were studied, nonlinearities in the excitation should be of great relevance in the production of sound, such as the generation of harmonics due to the saturation of the jet oscillations and an antisymmetric jet impact, and the losses due to vortex shedding at the labium. Moreover, noise produced by turbulence is a major aspect of this kind of instrument that deserves further investigation.

The experimental routine and the image processing techniques developed in this thesis can be applied to the study of other flue instruments, maintaining conditions very close to those of normal playing. A simple recommendation for further experiments would be to increase the size of the sample of each set of images. This would provide more information to each aggregated image, which should help smoothing the graphic noise of turbulence. This in turn should improve the quality of the detection of the median line of the jet and thus of the phase vector ϕ_η, providing a more accurate estimation of the phase velocity c_p.

2. SPECIFIC FEATURES OF A CLOSED-END PIPE BLOWN BY A TURBULENT JET: AEROACOUSTICS OF THE PANPIPES

2.1. Introduction

Many flute-like instruments from pre-Hispanic Latin America, especially those from the Andes region, share at least one common attribute: a resonator with a closed end. The most widespread species is the siku (also called zampoña, a name introduced by the Spaniards). The siku consists of several cylindrical stopped pipes attached together (Figure 2.1). Its operation is similar in principle to that of stopped tubes in organ pipes or to that of Western panpipes. While the the aesthetic emphasis in Western music is placed mainly on the organization of pitches, Andean musical excellence relies on the construction of a specific collective timbral texture which varies depending on the specific local culture and the particular type of festivity (de Arce, 1998). One key factor in the determination of this texture is the ceremonial character of the music; performances take place in open spaces, which requires loud sounds. Accordingly, pipes are blown with an extremely high jet flux. This results in the development of turbulence, associated with a strong wideband noise, both of which determine to a large extent the sound character of these instruments.

Most flute-like instruments whose sound production mechanisms have been well studied have open-open resonators and are commonly blown with laminar jets (Fabre et al., 2012); such is the case of the transverse flute, the recorder, and the organ pipe. Acoustics and fluid dynamics in stopped pipes have received comparatively little attention. In open-open pipes, the jet oscillates around the labium while the mean part of the entering jet (averaged over one period) induces a static flow through the pipe. Conversely, mass conservation in a stopped tube requires that the mean part of the jet flowing into the pipe must exit via the same place it entered: the blowing end. This results in a static component of the pressure gradient along the pipe and a subsequent steady component of the flow directed cross-stream to the jet. The jet flowing towards the labium crosses this area where it is deflected by the interaction with the crossflow (Figure 2.2).

FIGURE 2.1. Traditional cane siku composed of two rows of stopped pipes of different lengths and diameters.

In contrast to the laminar case, turbulence induces a rapid spreading and slowing of the jet, which affects the velocity of convection of the acoustic perturbations; more specifically, it may affect the delay of convection of the perturbations from the flue exit to the labium, an important parameter for the auto-oscillation balance.

This paper is structured as follows: Section 2.2 presents acoustic models in stopped pipes, including implications of turbulent jets and jets in crossflow. Fluid dynamic and acoustic models are developed for the purpose of interpreting data gathered from experiments on a laboratory replica of a siku. Possible modifications of the traditional flute model are also explored. Section 2.3 presents the experimental setup that makes it possible to obtain flow visualizations and pressure traces. Experiments are designed to test whether these types of instruments tolerate a wider range of control parameters (jet velocity, jet axis direction, and jet-labium offset) in order to produce stable oscillations. The results of these experiments are discussed in Section 2.5.

2.2. Modeling Stopped Pipes Excited by Turbulent Jets

While turbulent jets and some aspects of stopped pipes have been studied independently, there is no evidence as to how their combination would modify the behavior of a real instruments. Stopped-pipe instruments seem to tolerate a wider range of jet velocities while remaining in the first oscillating mode. Furthermore, it has been observed that the

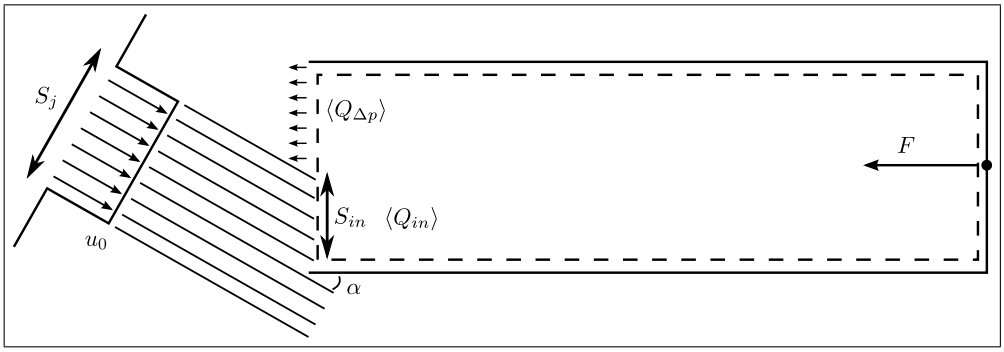

FIGURE 2.2. Idealized scheme of a stopped pipe. Part of the flow goes into the resonator building up the pressure inside and creating a cross-stream that comes out from the tube and interacts with the jet.

joint effect of turbulence and the steady crossflow may alter oscillations in the jet (Nolle, 1998; de la Cuadra et al., 2007) and its velocity profile.

Figure 2.3 shows a scheme of the instrument with the variables utilized to describe its operation. The pressure difference between the mouth of the flautist and the channel exit leads to the formation of a jet. The air flows through the short channel between the lips of the player and crosses a window of length W before reaching the labium. In resonant operation, this jet emerges within an acoustic field which perturbs the jet, mostly at its flow separation points at the flue exit (Fabre et al., 2012). Due to the intrinsic instability of the jet, this perturbation becomes amplified as it travels downstream. This results in a sinuous motion of the jet wave that is phase-locked to the acoustic oscillations. When the wavy perturbation reaches the labium, the separation of the jet into two flows with complementary phases is usually described as an acoustic pressure source—a driving force for the column of air inside the resonator. The resonator amplifies the source near its resonant frequencies, creating the acoustic field, which closes the feedback loop.

Sound production in flute-like instruments is commonly modeled using lumped elements, where the interaction between successive elements in the loop is assumed to be local. This approach has been discussed in several papers and has been verified by numerous experimental studies (Coltman, 1968; Elder, 1973; Fletcher, 1976; Verge et al., 1994; Fabre & Hirschberg, 2012). Accordingly, our analysis is separated in two: the Resonator

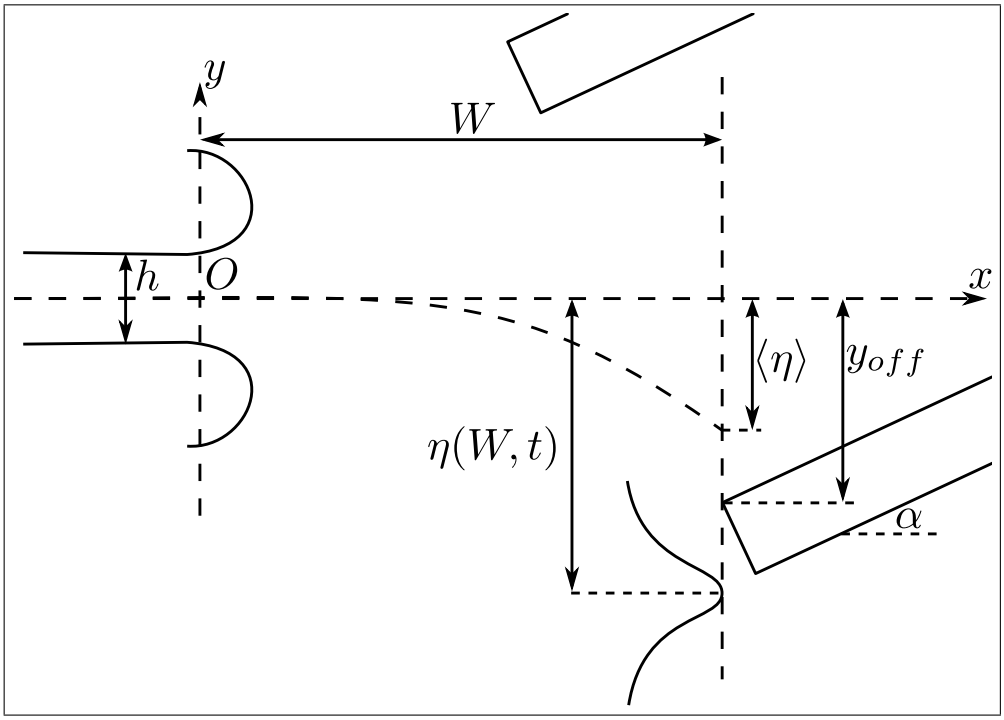

FIGURE 2.3. Schematic view of the excitation part of a siku. The jet emerges from the "lips" at O, crosses the window of width W while being bent along the mean jet centerline $\langle\eta\rangle$ by flow recirculation. The x-direction is defined as the distance from the lip opening along the axis of the flue channel. The geometrical blowing conditions are characterized by the offset y_{off} between the jet axis and the labium, and the angle α between the jet axis and the pipe axis. During the auto-oscillation, the jet centerline $\eta(x,t)$ oscillates around its mean deviation $\langle\eta\rangle(x)$.

and the Excitation. Finally, the implications of the interaction of the two lumped elements in the real instrument are presented.

2.2.1. The Resonator

2.2.1.1. Static Pressure Inside the Pipe

A model for the static pressure build up in the pipe Δp is developed based on mass and momentum continuity along the pipe axis. For the analysis, a non-oscillating and inviscid—i.e., non-spreading—jet is assumed; the velocity profile is considered to have a top-hat shape. A smoother velocity profile would not fundamentally affect the following description, but it would result in a more complex set of equations. Oscillations are removed by averaging out all quantities over one period.

The flow going into the pipe over one period $\langle Q_{\text{in}} \rangle$ depends on the total flow coming from the flue $Q_0 = u_0 S_j$, the section $S_{\text{in}} = \sigma S_j / \cos\alpha$ of the fraction σ of the jet volume flux that enters the pipe, and the angle of the jet α:

$$\langle Q_{\text{in}} \rangle = \iint_{S_{\text{in}}} \mathbf{u} \cdot \mathbf{ds} = \sigma u_0 S_j, \tag{2.1}$$

with S_j the section of the jet as sketched in Figure 2.2.

The flux going out of the pipe due to recirculation is:

$$\langle Q_{\Delta p} \rangle = S_{\Delta p} u_{\Delta p}, \tag{2.2}$$

where the velocity of the outgoing flux $u_{\Delta p}$ is assumed to be uniform on the section $S_{\Delta p} = S_{\text{pipe}} - \sigma S_j / \cos\alpha$. Considering the mass continuity equation $\langle Q_{\text{in}} \rangle = -\langle Q_{\Delta p} \rangle$ yields

$$u_{\Delta p} = -\frac{\sigma S_j u_0 \cos\alpha}{S_{\text{pipe}} \cos\alpha - \sigma S_j}. \tag{2.3}$$

The momentum continuity equation along the pipe axis for an incompressible flow is:

$$-\rho_0 \langle Q_{\text{in}} \rangle u_0 \cos\alpha - \rho_0 \langle Q_{\Delta p} \rangle u_{\Delta p} = F, \tag{2.4}$$

where F is the force exerted by the bottom of the pipe on the fluid. Using Eqs. (2.1) and (2.3) and expressing the force as a difference in pressure, relative to the surrounding pressure, $\Delta p = -F/S_{\text{pipe}}$ yields

$$\frac{\Delta p}{\rho_0 u_0^2} = \frac{\sigma S_j \cos^2\alpha}{S_{\text{pipe}} \cos\alpha - \sigma S_j}. \tag{2.5}$$

This rough estimation of the pressure build up at the closed end will be compared to measurements introduced in Section 2.5.

2.2.2. The Excitation

It has been suggested (Fletcher, 2005) on theoretical grounds that the fluid dynamic balance in stopped pipes produces an auto-direction effect of the jet towards the labium. In other words, there is no need to aim the jet sharply at the labium; this makes it easier to produce a sound.

Just as in open-open tubes, the flow going into a stopped pipe Q_{in} can be decomposed into its mean $\langle Q_{\text{in}} \rangle$ and oscillatory Q'_{in} components. However, in this case the mean flow $\langle Q_{\text{in}} \rangle$ should exit through the same place it entered: the blowing end. This results in a crossflow with a static component that interacts with the jet, and a static pressure build up Δp at the closed end. Both aspects are analyzed in the following sections.

2.2.2.1. Jets in Crossflow

Jets in crossflow have been studied by a number of authors (Muppidi & Mahesh, 2005; Plesniak & Cusano, 2005; Cambonie, Gautier, & Aider, 2013; Smith & Mungal, 1998; New, Lim, & Luo, 2006, 2003) in the context of their work on industrial applications. In the case of the siku, the crossflow is generated by the jet itself and corresponds to the recirculation of the injected mean flow $\langle Q_{\text{in}} \rangle$. The ratio r, defined as the jet central velocity over the crossflow velocity, is greater than 1 for the sikus, since the jet cross section is smaller than or equal to the opening of the pipe.

For such a ratio, the flow might be slightly affected ($r \gg 1$) or strongly perturbed ($r \sim 1$). In the latter case, shear layers instabilities increase from the flow junction area (near the nozzle exit) to an extremely unsteady flow area (Smith & Mungal, 1998). The development of the shear layer instabilities makes the momentum of the jet and the crossflow—initially different—to mix while traveling downstream. In particular, turbulence induces a momentum transfer. Shear layer instabilities are associated with a large scale vortex motion with limited momentum transfer to the surroundings. This mixing has been shown to be responsible for a greater mean deflection of the jet. Thus the sharper the shear layer, the more deflected the jet (New et al., 2006). The shape of the flue exit is also a crucial parameter that affects the development of the shear layer instabilities (New et al., 2003), and thus the mean deflection.

In most configurations found in the literature, the crossflow is assumed to be fully developed in a semi-infinite space; i.e., the boundary layer on the plane wall from which the jet emerges is self similar. In the case of the siku, the geometry of the junction area is relatively intricate and varies from one musician to another. Moreover, the information

usually studied, such as the modification of the jet velocity profile or the development of different kinds of vortices, is not necessary for the level of accuracy required by the present model. Hence, the effect of the crossflow is assumed to be described only by a mean deflection of the centerline $\langle\eta\rangle$ on top of which oscillations η' take place. Thus, the total displacement of the centerline as a function of the distance x from the lip opening is:

$$\eta(x,t) = \eta'(x,t) + \langle\eta\rangle(x), \tag{2.6}$$

where the mean jet deflection is commonly described with the x dependence (Muppidi & Mahesh, 2005)

$$\frac{\langle\eta\rangle}{rh} \sim \left(\frac{x}{rh}\right)^{\delta}. \tag{2.7}$$

According to different configurations found in the literature, the order of magnitude of the amplification coefficient δ is greater than, but of the order of, 1.

2.2.2.2. Jet Spreading and Slowing

A jet emerges at $x = 0$ with a velocity profile contingent on the history of the flow in the formation channel and on the shape of the flue exit. If the channel is short enough, the profile will assume a top-hat shape. The jet gradually smoothens due to the viscous entrainment of the surrounding fluid. At a distance l_e from the flue, the jet is considered to be fully developed and assumes a self-similar velocity profile. From there onwards, the self-similarity of the velocity profile yields :

$$u(x,y) = u_{\text{max}}(x) f(y/b(x)), \tag{2.8}$$

where f is the self-similar profile and where the characteristic vertical distance b and the centerline velocity u_{max} are both functions of the distance x; they describe the spreading and the slowing of the jet, respectively.

In turbulent jets, both the spreading and slowing behave different from laminar jets (Tritton, 1988), affecting the velocity profile and the phase velocity of the perturbation c_p. Turbulent viscosity partially explains the fact that turbulent jets dissipate energy more rapidly than laminar jets.

In the case of fully developed turbulent free jets (Tritton, 1988) , x-momentum conservation implies bu_{max}^2 =constant while due to the absence of other length scale b/x =constant, so that: $b \sim x$ and $u_{max} \sim b^{-1/2} \sim x^{-1/2}$. Based on the observations of several authors (Thwaites & Fletcher, 1980), the centerline velocity is assumed to be constant prior to l_e. This leads to:

$$u_{\text{max}}(x) = \begin{cases} u_0 & \text{if } x \leq l_e \\ u_0\sqrt{\frac{l_e}{x}} & \text{if } x > l_e \end{cases}, \tag{2.9}$$

where u_0 is the centerline velocity of the initial velocity profile.

As the jet evolves in a crossflow it changes its velocity distribution due to momentum transfer, and its profile may significantly differ from the self-similar shape. However, the crossflow is assumed to be relatively weak as compared to the jet ($r \gg 1$), so that the jet is well described by the self-similar assumption.

2.2.2.3. Jet Instabilities

Work on the linear stability analysis of infinite parallel flows was initiated by Rayleigh. Despite the unrealistic assumptions of his analysis, it provides some insights into the instability mechanisms. Basically, a time harmonic excitation gives rise to two harmonic unstable modes, varicose and sinuous, defined by a symmetric and antisymmetric displacement of the two shear layers (Mattingly & Criminale, 1971). In flute-like instruments the jet emerges cross-stream to the acoustic velocity field: the sinuous mode is dominant because of the strong antisymmetric excitation.

The relevant parameters provided by the stability analysis of parallel flows are the phase velocity c_p and the spatial growth rate α_i of the time-excited perturbation as functions of the Strouhal number and the self-similar velocity profile. The former determines

the convection delay of the perturbation and thereby the oscillating frequency. The latter is directly related to the amplification of the oscillation and therefore to the triggering of non-linear processes. For spreading jets, as the velocity profile evolves along the downstream direction, the two parameters c_p and α_i become functions of the downstream distance x too (Crighton & Gaster, 1976). However, this level of accuracy exceeds the one in standard flute-like instrument modeling, where c_p and α_i are typically assumed constant, even with respect to the Strouhal number.

For laminar jets, experimental investigations validated the linear description of the perturbation, as a propagative transverse oscillation of the jet centerline (de la Cuadra, 2005):

$$\eta'(x,t) = e^{\alpha_i x}\eta_0(t - x/c_p), \tag{2.10}$$

where the receptivity η_0 is a key parameter which reflects the modulation of the shear layers at the flow separation points of the jet due to the acoustic field. The receptivity is an empiric formulation that does not have a physical meaning: the jet centerline cannot be displaced at $x = 0$. Furthermore, the formula is valid only for a few characteristic distances h downstream. However, it shows reasonably good agreement with experimental data using

$$\frac{\eta_0}{h} = \frac{v_{\text{ac}}}{u_0}, \tag{2.11}$$

where v_{ac} is the harmonic transverse acoustic velocity at the flue exit. The parameters of convection velocity and amplification of the jet wave are defined as $c_p = \gamma u_0$ and $\alpha_i = \beta/h$, respectively, where $\gamma \sim 0.4$ and $\beta \sim 0.3$ in laminar jets (Auvray et al., 2012).

Studies on the instabilities of jets describe the transition from laminar to turbulent regime as triggered by the spatial amplification of spontaneous oscillations due to the instabilities in the shear layers (Tritton, 1988). In the case of synchronized oscillations, such as in edge-tone or flute configuration, turbulence may be triggered by the spatial growth of the perturbed jet. Indeed, when the amplitude of oscillation is large enough, nonlinear mechanisms are predominant. The vortices formed by the Rayleigh instability give rise to large scale structures in the turbulent flow.

Using particle image velocimetry on a turbulent jet in an edge-tone configuration, Lin and Rockwell (Lin & Rockwell, 2001) showed that large-scale patterns of vorticity are phase-locked with the measure of pressure on the tip of the edge. These large-scale patterns are of the same order as the hydrodynamical wavelength in a laminar case. Thus, the associated acoustic frequency is expected to be of the same order as the frequency in a laminar edge-tone. Lin and Rockwell also observed small-scale patterns of vorticity with no specific phase relation with the jet oscillation nor with the pressure measurement. These patterns of much smaller hydrodynamical length scale contribute to the production of broadband noise, a characteristic of turbulence: high frequency broadband noise with an absence of phase correlation with the large scale oscillation.

As for the modeling of the spreading and slowing of the jet, the contribution of the non-correlated vorticity patterns can be integrated into a simple model—similar to the laminar case—with an effective viscosity due to small-scale eddies interaction. Disregarding small fluctuations, the transverse displacement of the jet is assumed to be well approximated by Eq. (2.10) with values of the critical parameters η_0, c_p and α_i, which may differ from those of the laminar case though they are expected to be of the same order of magnitude (de la Cuadra et al., 2007).

Oscillation of turbulent jets forced by an acoustic transverse excitation have already been studied by Thwaites et. al. (Thwaites & Fletcher, 1980, 1982), and de la Cuadra et. al. (de la Cuadra et al., 2007). They found that the phase velocity roughly behaves as $c_p \sim x^{-1/2}$. Concerning the amplitude of oscillation, the initial part of the jet is well approximated by an exponential growth with a factor $\beta \sim 0.4$. Beyond a certain length, the amplitude of oscillation will exceed the half-width, and the growth of the perturbation will no longer be linear (Thwaites & Fletcher, 1982).

2.2.2.4. Overblowing

The delay of the perturbation on the jet is critical in determining the oscillating frequency (Coltman, 1968). Sound production is optimal for a convection delay τ_c close to half the oscillating period T (Fabre & Hirschberg, 2012; Auvray et al., 2012). Since

TABLE 2.1. Strouhal ranges that allow oscillation from different experimental results, on different types of flute.

	Lower limit	Optimal value	Upper limit
Verge *et al.* (1997)	0.07	0.17	0.25
Ségoufin *et al.* (2000)	0.07	-	0.25
de la Cuadra *et al.* (2008)	0.07	-	0.3
Auvray *et al.* (2012)	0.06	0.20	0.4

the perturbation travels at about γu_0, sound production is optimal for a Strouhal number $St_w = fW/u_0$ close to $\gamma/2$ (when $\tau_c = W/\gamma u_0$ equals $1/2f$).

Modifications on the total delay, caused by a slower convection of the perturbation in turbulent jets, also affect the overblowing mechanisms of the instrument. Oscillations are possible within a critical range around the optimal value. Values of the Strouhal critical range in experimental results from various authors are indexed in Table 2.1. The lower limit of the Strouhal number corresponds to the critical value at which the system overblows, roughly close to a third of the optimal value. It should be noted that the mechanisms that trigger the regime change have not been fully understood, although some of them have been identified (Auvray et al., 2012), and that the evidence presented here is of an experimental nature.

When the convection delay becomes too small because of an increase in the jet velocity, the Strouhal number decreases below its critical lower limit and the system changes its oscillating regime to match the next mode of the resonator. In other words, in an open-open pipe sounding in its first regime, an increase in the jet velocity beyond the critical value would result in an overblowing of the system on the second mode, thereby doubling the frequency. Thus, the balance of delays remains within the critical range, as does the Strouhal number.

It is well known that in stopped pipes the frequency ratio of the resonances are approximately in the ratio of the odd integers, with the result that, when the jet frequency is close to the first resonance, odd harmonics fall near resonances and become significantly stronger than the even harmonics. Moreover, overblowing a stopped pipe would produce a

mode shift, jumping to a frequency close to three times that of the fundamental. One might expect the critical range to be extended due to the enlargement of this frequency interval.

The balance of delays may also be modified by one of the effects of the turbulence: the spreading of the jet is expected to modify the phase velocity of the perturbation (Crighton & Gaster, 1976), and thereby the convection delay. The total delay should be integrated over the window distance W with the local phase velocity γu_0 where γ is a function of the downstream distance x. However, this description exceeds the accuracy of current models since the exact evolution of the jet velocity profile is required to compute the local phase velocity. A more general approach which still accounts for the slowing of turbulent jets and finds support in experimental observations (Thwaites & Fletcher, 1980; de la Cuadra et al., 2007) would be to consider an effective Strouhal number defined as:

$$St^* = \int_0^W \frac{f dx}{u_{\max}(x)} = \int_0^{l_e} \frac{f dx}{u_0} + \int_{l_e}^W \frac{f dx}{u_0 \sqrt{x/l_e}} = \frac{f l_e}{3u_0}\left(2\left(\frac{W}{l_e}\right)^{3/2} + 1\right). \tag{2.12}$$

St^* will be used as an indicator of the regime changeability.

2.3. Experiment

A laboratory replica of a siku was built with the modifications necessary to allow proper visualization and further analysis of images. The experiments seek to validate the parameters of the models proposed in Section 2.2, including a detection of the jet centerline $\eta(x,t)$ for the analysis of the mean deflection $\langle\eta\rangle$ and the instability jet wave $\eta'(x,t)$, and the establishment length l_e. An acoustical analysis of the sounds obtained is also included.

2.3.1. Setup

The control parameters of the experiments are the jet-pipe angle α and the Reynolds number $Re = u_0 h/\nu$, varied through the jet velocity u_0—for a flue of height h and a fluid of viscosity ν (for CO_2, ν =8.1×10^{-6} m^2/s). The pipe is blown with pure CO_2 for visualization purposes.

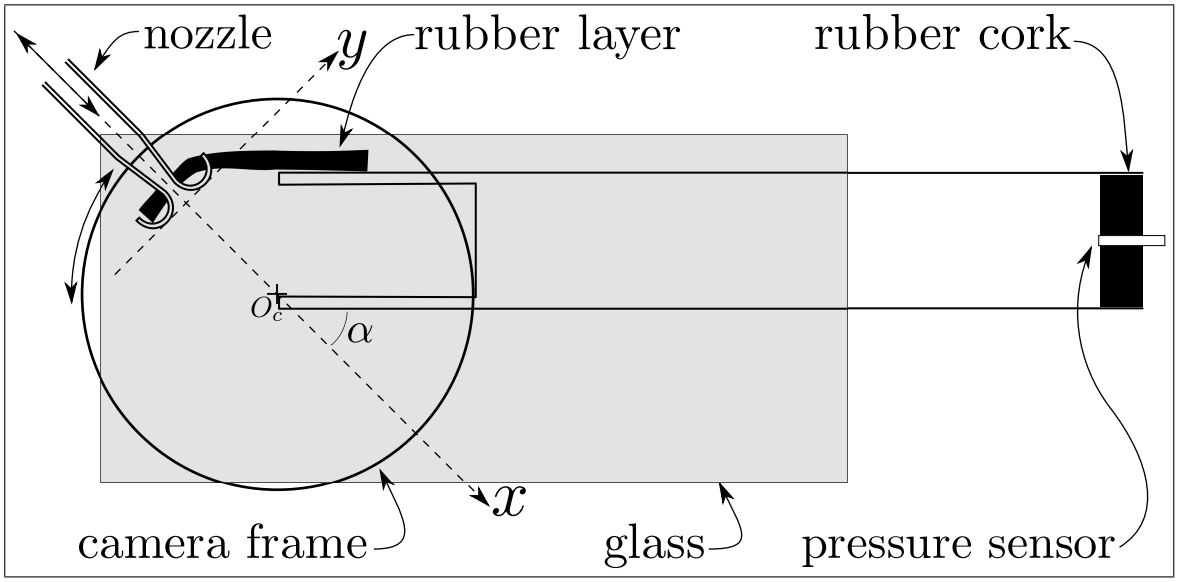

FIGURE 2.4. Sketch of the experimental setup: Pipe and nozzle as seen by the camera through the glasses. The nozzle can rotate around the center O_c and can be translated along the x axis.

The pipe is an aluminium tube with a square section: an inner cross-sectional area of 0.67 cm^2 and an inner length $L_{\text{pipe}} = 9.76$ cm. The pipe is assumed to be uniformly filled with pure CO_2, this provides a fundamental frequency in CO_2 of $f_0 = c_0/4L_{\text{pipe}} = 686$ Hz with the speed of sound $c_0 = 268$ m/s. The stopped end is closed by a rubber cork with an Endevco dynamic pressure sensor model 8507C-2 mounted flush on it. In the region near the open end, two opposite walls were cut off and replaced with two larger pieces of transparent glass to make a visualization area (see Figure 2.4).

The flue is made of a cylindrical brass tube of inner diameter 4.8 mm whose end has been flattened, cut and bent to resemble lips. The flue exit is 7 mm wide and $h = 0.7$ mm high, yielding a cross-section $S_{\text{flue}} \simeq 4.9$ mm^2. A 1 cm wide, 5 cm long, and 3 mm thick rubber piece was used to seal the gap between the flue and the edge of the pipe opposite the labium, an area that is normally filled by the jaw or lower lip of the instrumentalist.

The pipe and the nozzle are mounted on a system that allows for the variation of the flue-labium distance W, and the jet-pipe angle α. The radius W, chosen empirically to give optimal sound production, is set at 9.3 mm.

The pure CO_2 jet is regulated using a Brooks mass flow controller. Between the controller and the nozzle the flow passes through a settling chamber of volume 2.5×10^{-3} m^3 where the velocity is taken to be zero and the pressure is measured using an Endevco dynamic pressure sensor model 8507C-2. The cavity is connected to the nozzle by a plastic tube of inner diameter $D = 6.2$ mm and length $L = 2.5$ m. This allows for a complete development and stabilization of the velocity profile in the tube; however, viscous losses are significant and cannot be disregarded. Consequently, a specific model is developed for the estimation of the velocity at the flue. The jet velocity is estimated by applying the law of Blasius. For a turbulent flow in a cylindrical pipe of length L, the pressure drop P_{drop} between the cavity and a point just before the constriction of the nozzle is given by (Schlichting & Gersten, 2004):

$$\frac{P_{\text{drop}}}{L} = \lambda \frac{\frac{1}{2}\rho_0 u^2}{D}, \tag{2.13}$$

where u is the centerline velocity just before the constriction of the nozzle, ρ_0 the density of the fluid (for CO_2, ρ_0 =1.8 kg/m^3) and $\lambda = 0.316 Re_D^{-1/4}$ the friction coefficient, with the Reynolds number $Re_D = uD/\nu$ and the viscosity ν. The jet centerline velocity at the nozzle u_0 can be estimated by applying mass conservation ($uD^2\pi/4 = S_{\text{flue}}u_0$) and energy conservation (Bernoulli) between the points just before and after the constriction.

In addition to the internal pressure measurements, a B&K 4938 microphone captures the radiated pressure at a point set 29 cm away from the labium (9 cm above the labium in the axial direction of the pipe, 19 cm in the direction perpendicular to the x-y plane, and 20 cm in the direction perpendicular to the pipe axis and parallel to the x-y plane).

Visualization is achieved by blowing CO_2 for all the experiments and using the Schlieren photography technique. Images are captured at 8 Hz with a shutter speed of 100 ns. Additionally, the camera provides an analog synchronizing signal independent of the pressure oscillation. A typical image of the experiment is shown in section 2.4. Since the pipe is saturated with CO_2, the mass gradient of the inner shear layer of the jet is less pronounced, causing a weaker contrast in the flow visualization.

2.3.2. Experiments

Each experiment covers the acquisition of 368 images ($\sim$ 46 sec) under steady conditions of the control parameters α and $Re = u_0 h/\nu$. A total of 20 measurements are performed, covering five jet angles (24°, 36°, 46°, 57° and 69°) and four Reynolds numbers ($\sim$ 2400, 3000, 4300, and 5200) corresponding to four jet velocities ($\sim$ 28, 35, 50 and 60 m/s). In all cases the jet has a laminar and a turbulent region, with a transition around 3 mm downstream from the flue.

All concluding remarks in this investigation are retrieved from this set of 20 experiments. Nonetheless, in an attempt to determine whether the jet auto-directs towards the labium, as suggested by Fletcher (Fletcher, 2005), three additional measurements were performed by shifting the offset $y_{\text{off}} \simeq 3$ mm, thus aiming the jet at the center of the bore. Using this configuration, three angles (24°, 36°, 46°) were tested with $Re \simeq 4300$ (jet velocity of $\sim$ 50 m/s).

For an average range of $Re \simeq$2400 to 5200, the variation of other relevant quantities is as follows: fluctuating pressure at the closed end p', 143 to 159 dB; radiated pressure, 75 to 93 dB; pressure difference in the pipe Δp, 40 to 240 Pa; pressure in the upstream cavity p_{cavity}, 1000 to 4500 Pa; and mass flow controller output, 1.4×10^{-4} to 2.9×10^{-4} m^3/s.

2.4. Images Processing

The images present several challenges from the viewpoint of the analysis. For instance, one of the control parameters is the jet-pipe angle, which means that the geometrical configuration changes constantly. Furthermore, the video frame rate is not synchronized with the oscillations of the jet, which also changes with each experiment. Thus, processing is needed to define a homogeneous window of observation, such as the one in Figure 2.3, and to synchronize the images with the acoustic signals in order to analyze the wavy perturbation of the jet.

The detection of the centerline of the jet is used to measure the quantities of the vertical displacement $\eta'(x,t)$. Small vortical structures produced by turbulence difficult this

detection, because they have a noisy pattern. Therefore, a cross-temporal filter is designed to reveal the structure of the jet in order for the detection algorithms to work properly.

2.4.1. Pre-Processing the Data

The camera frame rate is much lower than the frequency of the jet wave (8 Hz and ∼690 Hz, respectively) so that sequential images do not follow the oscillating motion of the jet. However, large-scale patterns of vorticity are phase-locked with the acoustic oscillations, as mentioned in Section 2.2.2.3. An algorithm was developed to label images with the instantaneous phase of the fluctuating pressure at the closed end p' at the moment of their capture. Thus, an array of images $I = [I_1, I_2, ..., I_N]$ is linked to a vector of phases $\phi = [\phi_1, \phi_2, ..., \phi_N]$ which are distributed uniformly in the interval $[0 - 2\pi]$. The array I and the vector ϕ are reordered so that $0 \leq \phi_1 \leq \phi_2 \leq ... \leq \phi_N < 2\pi$.

Small scale patterns of vorticity have no relation to the acoustic oscillations and behave randomly in consecutive images of I. This complicates the analysis from the viewpoint of the detection of the centerline. By aggregating information from phase adjacent images, recurrent structures are highlighted and others decomposed. The following pixel-by-pixel procedure combines images in I using a Gaussian-weighted average around a phase φ. The result is called an aggregated image $\tilde{J}(\varphi)$:

$$\tilde{J}(\varphi) = \frac{\sum_{k=1}^{N} I_k \cdot c_k(\varphi)}{\sum_{k=1}^{N} c_k(\varphi)}, \tag{2.14}$$

where the coefficients $c_k(\varphi)$ are defined as

$$c_k(\varphi) = e^{-\frac{1}{2}\left(\frac{\phi_k - \varphi}{\zeta}\right)^2}, \tag{2.15}$$

and the parameter ζ adjusts the spread of the curve.

A reconstruction in time of a period of oscillation of the jet wave is made in M uniform frames $0, \frac{1}{M}2\pi, ..., \frac{M-1}{M}2\pi$. Aggregated images $\tilde{J}(\varphi)$ are computed by forcing φ to match those intervals, and single-shot images J are picked out as uniformly as possible from ϕ.

For the following analysis, parameters are set to $\zeta = 8.4°$ and $M = 32$.

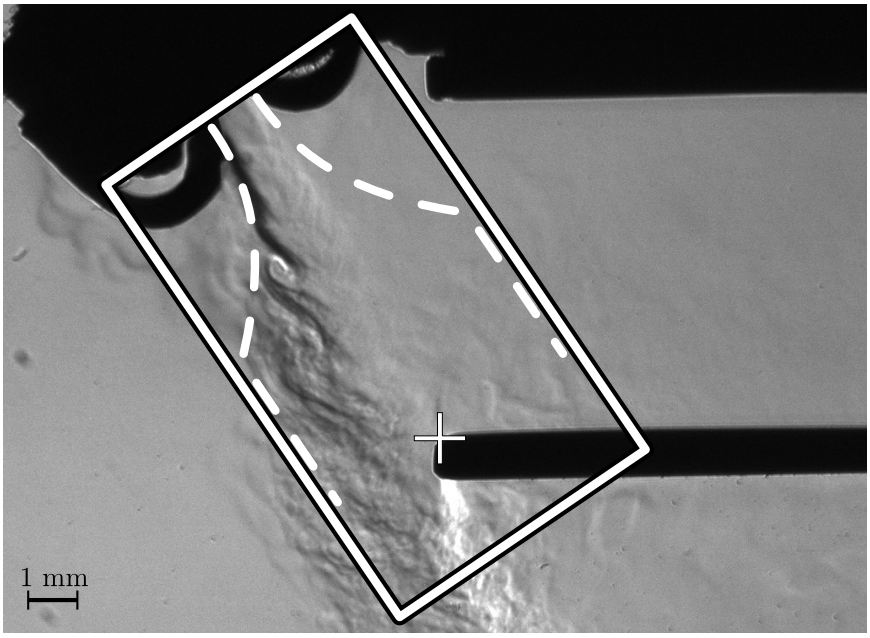

FIGURE 2.5. Typical image captured by the camera for the blowing condition (Re,α) = (3000,57°). The rectangle is the window of observation, the dashed line is the mask used for the detection of the jet transverse oscillation, and the white cross is the center of rotation on which the jet axis is centered.

Prior to the subsequent analysis of the jet's centerline, the main axes of the model (see Figure 2.3) have to be defined. To this effect, an x-axis and a representative point marking the origin of the jet must be found. The former cannot be deduced from images for these contain information on the vertical displacement. However, the total average of images in array $\tilde{J}$ is expected to provide a better idea of the initial orientation of the jet. A line is adjusted to fit the direction of the early development of the jet, and the origin is placed at the edge of the flue. In order to generalize the axes definition for different geometrical configurations, it is necessary to develop an alignment algorithm that uses the structure of the nozzle as an invariant marker of the orientation of the jet. The algorithm is based on the technique called 'image registration", which maximizes the mutual information between images (Maes et al., 1997), and yields the translation and rotation of the nozzle structure relative to a reference. Thus, the axes need to be defined for one experiment only, and the results are extrapolated to the rest by means of the alignment algorithm.

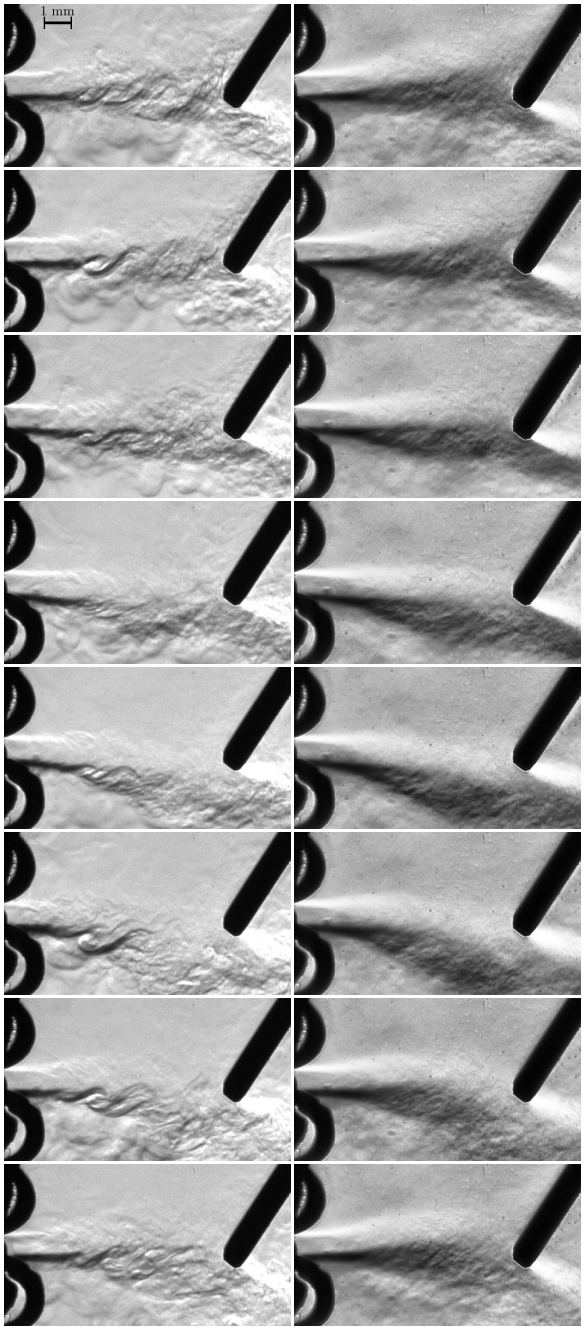

FIGURE 2.6. Time series of jet oscillation for one blowing condition (Re,α) = (3000,57°). Left column: Single-shot images. Right column: Aggregated images. (from top to bottom: t/T = 0, 1/8, 2/8, 3/8, 4/8, 5/8, 6/8, 7/8 – the phase reference corresponds to the zero increasing pressure at the bottom of the pipe).

2.4.2. Jet Centerline Tracking: Relative Displacement

De la Cuadra (de la Cuadra et al., 2007) proposed an algorithm for measuring the vertical displacement of a jet based on the cross-correlation between analog gray profiles of images at consecutive time frames. The method uses a reference image and cross-correlates the rest to it. Thus, displacements obtained are relative to the one in the reference image. A brief summary of the algorithm is provided below.

The cross-correlation of a vertical gray profile $l(y, x, t)$ at a distance x from the flue and time frame t is

$$X(y, x, t) = \int_{-\infty}^{\infty} l(y - \tilde{y}, x, t_{ref}) l(\tilde{y}, x, t) d\tilde{y}. \tag{2.16}$$

$X(y, x, t)$ will have a maximum for a lag $\tilde{y}$ that makes both profiles match best. Then, the shift of that maximum from the center of the vector is taken as the relative displacement $\tilde{\eta}(x, t)$. This is often of the order of a few pixels, so that the parabolic interpolation of the three highest values is used to increase resolution of the peak detection.

This operation is repeated for the M time frames and for the entire discrete window of N_W points ($x \in [0, N_W - 1]$). The result of the algorithm is the $M \times N_W$ matrix of relative displacements whose first row is made up of zeros to represent the unknown displacement of the reference image.

2.4.3. Jet Centerline Tracking: Absolute Displacement

In open-open pipes, the mean deflection of the centerline $\langle \eta \rangle$ coincides with the x-axis. This makes it possible to correct the reference displacement by forcing the mean value of the columns of $\tilde{\eta}(x, t)$ to zero. In stopped pipes $\langle \eta \rangle$ varies with x; hence, the position of the jet in the reference image must be obtained separately and it must then be subtracted from $\tilde{\eta}(x, t)$.

The morphology of the jet in aggregated images is characterized by two velocity profiles (a top-hat shaped profile at the exit of the nozzle, and an auto similar profile a distance away from it). First, the shear layers are two distinguishable boundaries of the jet, and after

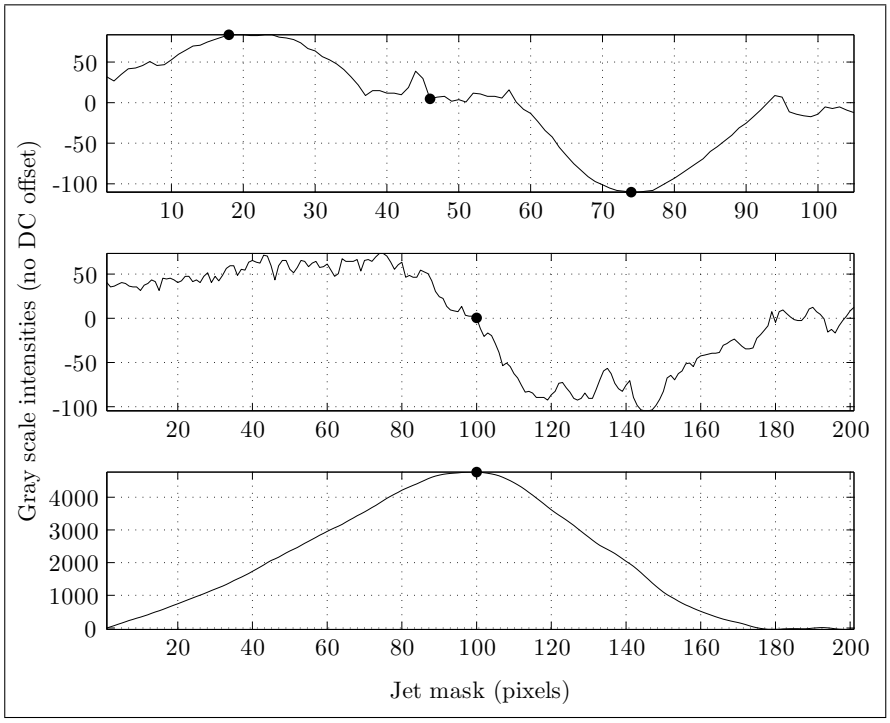

FIGURE 2.7. a) Gray profile in laminar region. b) Gray profile in turbulent region. c) Integral of b.

a certain distance of establishment l_e, these boundaries collapse in the centerline. Two algorithms based on vertical gray profiles run in the regions $x \in [0, \tilde{l_e} - 1]$ and $x \in [\tilde{l_e}, N_W - 1]$, respectively, where the distance $\tilde{l_e}$ is a heuristic estimation of l_e used only for this transition. Despite the gradual nature of the diffusion of the shear layers, the change is assumed –without compromising the results– to be discrete.

In the first region, a profile $l(y, x, t)$ looks like Figure 2.7 (upper graph). Maximum and minimum points are good indicators of the boundaries of the jet, and the centerline is assumed to lie at the center of both.

A gray profile in the second region looks like Figure 2.7 (middle graph). Visualization is now characterized by noise, so that the former criteria of detection are no longer valid. The shape of $l(y, x, t)$ suggests that a larger scale approach is necessary, such as the area below the curve. This operation acts as a low pass filter, reducing the effects of noise. The

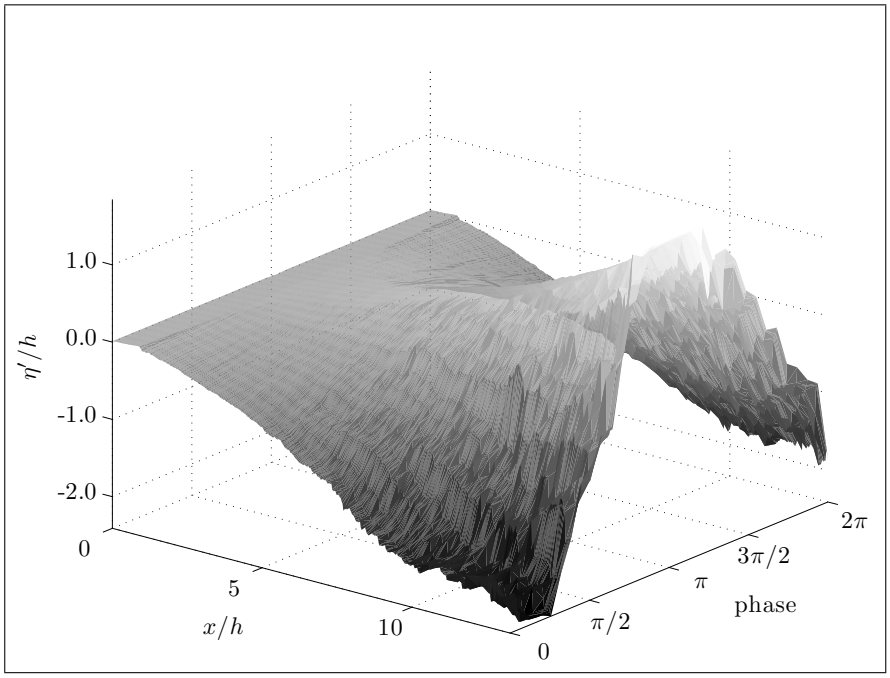

FIGURE 2.8. Three-dimensional representation of the jet transverse oscillation $\eta(x,t)$ versus the M=32 time frames and the distance from the nozzle x for the case (Re,α) = (4300,36°).

integral of the gray profile, starting from the first intensity value, is shown in Figure 2.7 (lower graph). The maximum of this curve marks the centerline.

An exponential fit to the combined results yields the absolute displacement of the reference image $\eta(x,0)$. Finally, the rows of matrix $\tilde{\eta}(x,t)$ have to be corrected by means of the operation:

$$\eta(x,t) = \eta(x,0) - \tilde{\eta}(x,t), \qquad \forall t \in [\![1, M-1]\!]. \tag{2.17}$$

A three-dimensional plot of the absolute displacement $\eta(x,t)$ is shown in Figure 2.8.

Detection in aggregated images is robust; the centerline can be tracked from the flue to the labium. Therefore, the analysis of the instability of the jet and the mean deflection will use these images. Contrarily, algorithms of detection in single-shot images perform poorly due to uncorrelated small-scale patterns of vorticity. This characteristic will be used to identify the establishment length at which the turbulence reaches the core of the jet.

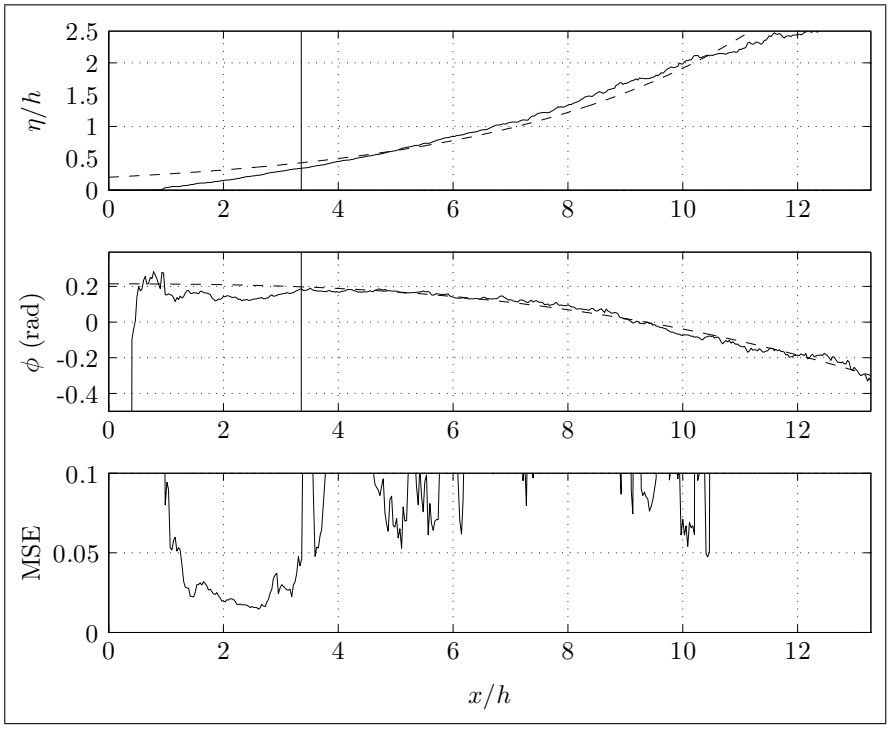

FIGURE 2.9. Amplitude, phase and MSE of the oscillation of the jet for one blowing condition: (Re,α) = (4300,36°). The vertical line is the estimation of the establishment length l_e based on the MSE.

2.4.4. Spatiotemporal Analysis of the Centerline

The static and oscillatory components of the columns of $\eta(x,t)$ represent the mean jet deflection $\langle\eta\rangle$ and the jet wave $\eta'(x,t)$, respectively. Fourier analysis of the columns of $\eta'(x,t)$ yields the amplitude $|\eta'|$ and the phase $\phi_{\eta'}$. The growth rate α_i is obtained from the fit of $|\eta'|$ using the function $\eta_0 e^{\alpha_i}$, as illustrated in Figure 2.9. The convection velocity is deduced from the phase of the wave $\phi_{\eta'}$, with the expression (Nolle, 1998) $c_p = \omega(d_x\phi_{\eta'})^{-1}$. c_p depends on the derivate of a noisy vector; thus, it cannot be obtained directly and requires a function to be fitted to $\phi_{\eta'}$ previously. In turbulent jets $c_p \propto x^{-\frac{1}{2}}$, thus $\phi_{\eta'} \propto x^{\frac{1}{2}}$. However, the data obtained is too irregular to generalize a result and requires further investigation. Nevertheless, a change of slope in $\phi_{\eta'}$ that coincides with the detection of the establishment length l_e is observed. In the laminar region, the slope seems to be linear, while in the turbulent region it is better approximated by a polynomial.

Small-scale patterns of vorticity reduce the performance of detection, especially in single-shot images. A measure of turbulence is the mean squared error (MSE) between the normalized columns of $\eta'(x,t)$ and their sinusoidal fit:

$$\text{MSE} = \frac{1}{M}\sum_{t=1}^{M}\left[\frac{1}{|\eta'|(x)}\eta'(x,t) - \cos\left(2\pi M^{-1}t + \phi'_{\eta'}(x)\right)\right]^2. \tag{2.18}$$

The MSE can be divided into three regions: forming, laminar and turbulent. Oscillations starts to arise in a region of length $x \sim h$ near the flue exit; this causes the detection to be highly irregular, having a large MSE. In the laminar core region the MSE quickly decreases due to a structured and cohesive jet. This state lasts until turbulence arises at $x/h \sim 3$–5, depending on the blowing conditions, where the MSE increases rapidly. This establishment length l_e can be easily identified, as shown in Figure 2.9 (lower graph), and it was detected heuristically.

2.5. Results

2.5.1. The Resonator

The pressure difference at the closed end of the tube Δp is compared to the model developed in the previous section (see Eq. (2.5)). Results are displayed in Figure 2.10. The pressure difference slightly increases as the angle decreases (i.e., as the jet aligns itself with the pipe axis). The prediction of the model overestimates the pressure decay with the angle but provides the same order of magnitude and the same trend. However, the model does not predict a Reynolds number dependence, though it was experimentally observed. The adjustable parameter σ has been set to 0.55 to match experimental observation, making it possible to estimate the fraction of the jet which enters the pipe and therewith the ratio r of the jet velocity over the crossflow velocity (see Eq. (2.3)): for all the experiments, r has been found to be of the order of 23 except for the three experiments where the offset $y_{\text{off}} \simeq 3$ mm, σ being set to 0.95.

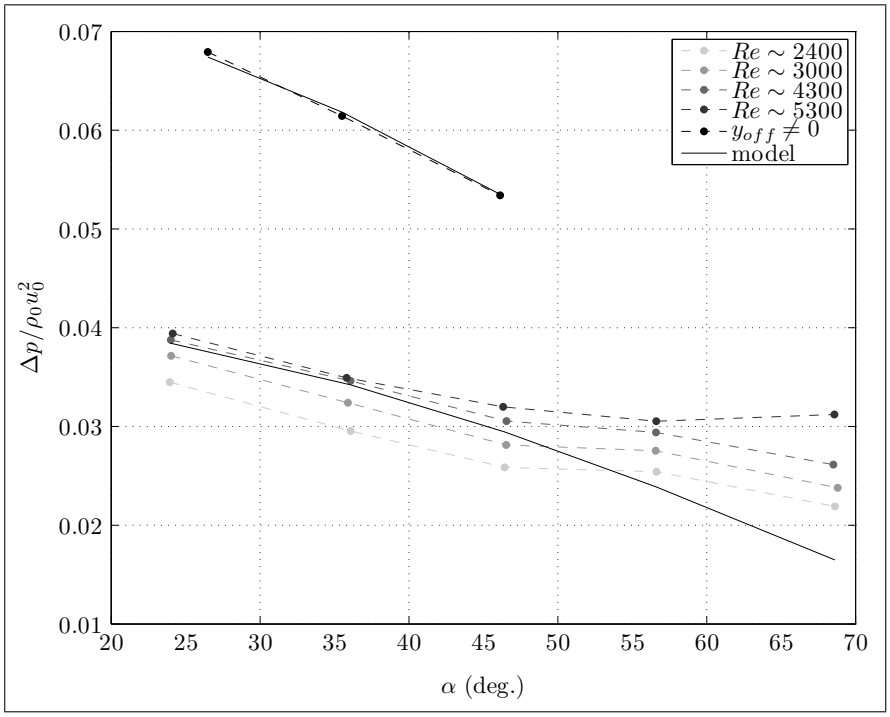

FIGURE 2.10. Dimensionless pressure difference at the closed end $\Delta p_{/}\rho_0 u_0^2$ versus angle of the jet α for different flow commands (solid line: model developed in Section 2.2.1.1; dashed line: experimental data). The parameter fraction of jet that enters the pipe σ is set to 0.55 for the case $y_{\text{off}} = 0$ and 0.95 for the case $y_{\text{off}} \neq 0$.

2.5.2. The Excitation

2.5.2.1. Jets in Crossflow

The detection of the instantaneous deflection of the centerline $\eta(x,t)$ using aggregated images is shown in Figure 2.11 (blue straight line). The mean deflection of the centerline $\langle\eta\rangle$ (red dotted line) is also shown and evidences the deviation from the x-axis of the average oscillation. Results of $\langle\eta\rangle$ show the expected behavior for a jet in a crossflow given by Eq. (2.7), but only in the first half of the jet. In the second half, the shifting tendency seems to cease; the mean position of the centerline remains in the vicinity of the displacement achieved in the first half. The jet deflection has been fitted with the function $\langle\eta\rangle/rh = a(x/rh)^{\delta}$ on the first half of the window ($x \in [0, W/2]$). Figure 2.12 shows values of δ. Except for the very critical case α = 69° (with jet almost orthogonal to the pipe axis), all the δ values are close to 2. No specific trend for δ with the Reynolds number,

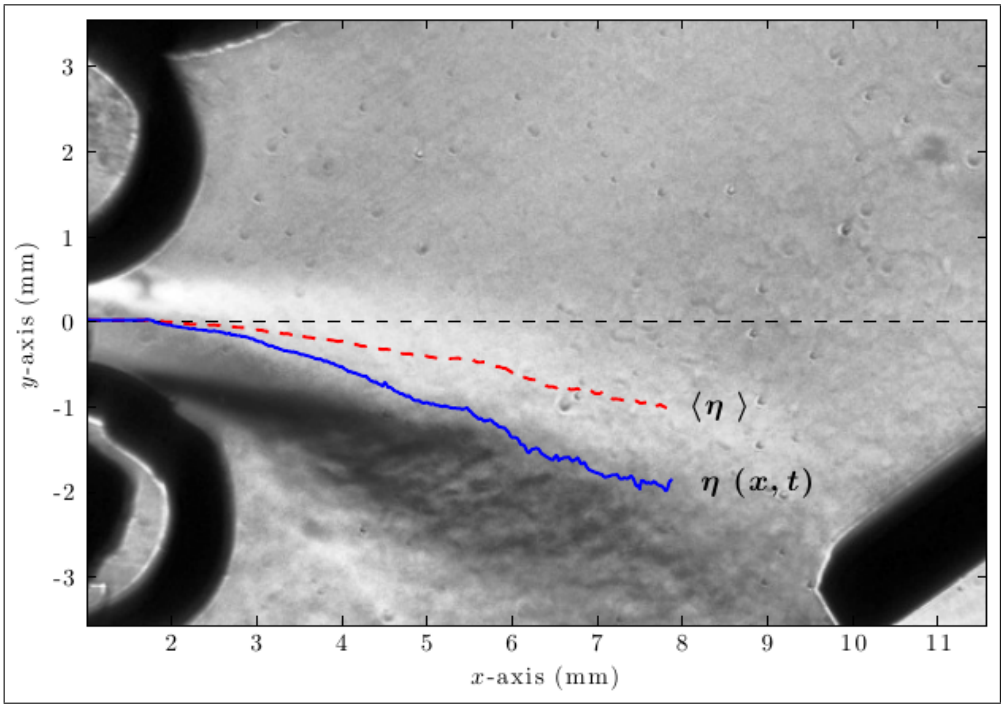

FIGURE 2.11. Detected instantaneous deflection $\eta(x,t)$ (blue straight line) and mean deflection $\langle\eta\rangle$ (red segmented line) of the centerline of the jet, for φ =146.25°, y_{off} ≃3 mm, and (Re,α)=(4300,36°).

nor with the angle α, has been found. This is remarkable since the characteristics of the jet-crossflow interaction are highly dependent on both parameters.

The total jet displacement at the labium is small, $\langle\eta\rangle(W) \simeq 0.35$ mm. Nevertheless, for the three experiments where the offset is changed to $y_{\text{off}} \simeq 3$ mm, the tendency $\langle\eta\rangle \sim x^{\delta}$ is maintained throughout the entire jet length. Values of δ for this case are also displayed in Figure 2.12. The total displacement is now $\langle\eta\rangle(W) \simeq 1$ mm, so that the jet does not oscillate around the labium but around a point two millimeters above it.

2.5.2.2. Jet Spreading and Slowing

In order to determine the position at which the jet is fully developed, l_e, an image analysis algorithm, has been implemented and is described in section 2.4.

Results of l_e are displayed in Figure 2.13 (upper graph). The turbulent mechanisms are triggered closer to the flue exit as the Reynolds number increases: from $l_e/h \sim 5$ for $Re =$

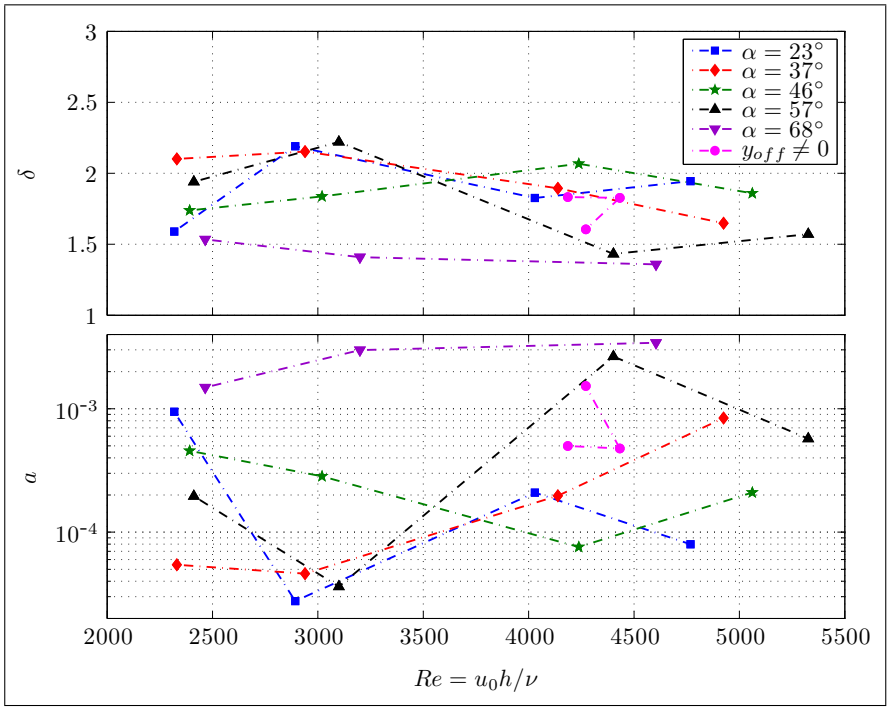

FIGURE 2.12. Coefficient δ of the steady deflection of the jet $\langle\eta\rangle/h = a(x/h)^{\delta}$ versus Reynolds number $Re = u_0 h/\nu$ for all the blowing conditions. If not specified in the legend, the offset y_{off} is null.

2400 to $l_e/h \sim 2$ for $Re = 5200$. No apparent relation to angle α or to the jet offset y_{off} is observed.

2.5.2.3. Jets Instabilities

The function $\eta_0 e^{\alpha_i x}$ is fitted to the wave amplitude data. The measured amplification factor $\beta = h\alpha_i$ is shown in Figure 2.14. The order of magnitude of the growth rate is the same as the ones found in the literature for turbulent jets (Thwaites & Fletcher, 1980, 1982; de la Cuadra et al., 2007). No specific trend with the Reynolds number Re or with angle α has been found. As already observed in these earlier studies, there is no difference between the laminar and turbulent regions. In addition, an interesting result was obtained for the three experiments where $y_{\text{off}} \simeq 3$ mm. In this case, the growth rate α_i is larger and shows a dependence on the angle.

Another parameter usually studied together with the amplification factor is the convection velocity c_p, deduced from phase of the wave $\phi_{\eta'}$ with the expression (Nolle, 1998)

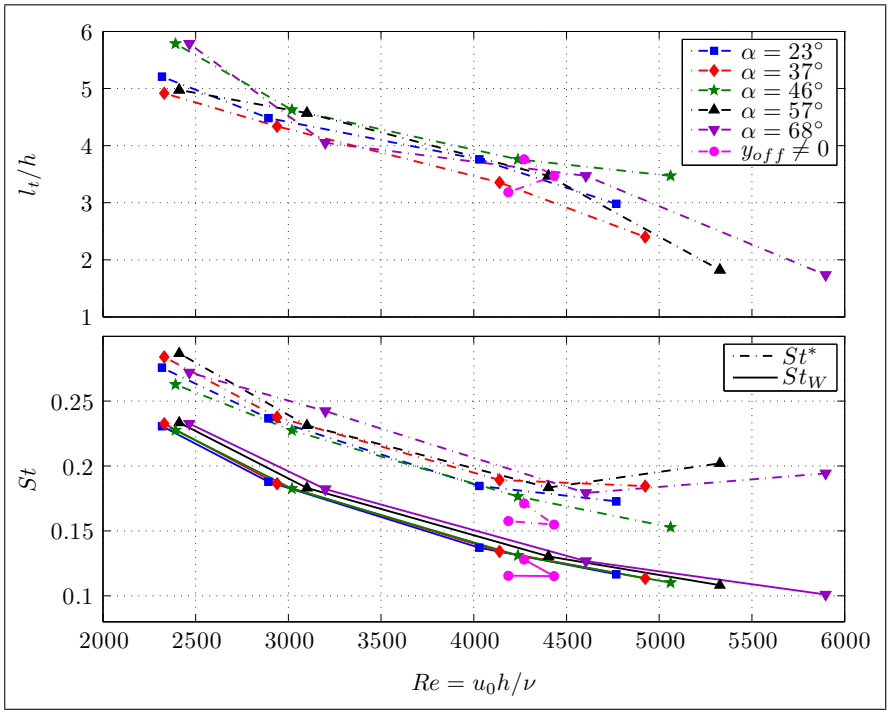

FIGURE 2.13. Dimensionless establishment l_e/h and Strouhal numbers $St_W = fW/u_0$ and St^* (see Eq. (2.12)) versus the Reynolds number $Re = u_0 h/\nu$ for all the blowing conditions. If not specified in the legend, the offset y_{off} is null.

$c_p = \omega(d\phi_{\eta'}/dx)^{-1}$. It provides information on the total delay, and thus on the ability of the system to overblow. As expected from the model, the rate of change of phase $d\phi_{\eta'}/dx$ behaves differently before and after the establishment length l_e. There is a change in the slope of the phase that coincides with l_e, reducing the phase velocity for the turbulent region. However, the phase data of the present experiment is too noisy (because of turbulence) to allow for a proper estimation of c_p. Only for a few of the experiments it was possible to deduce information on c_p, which was estimated to be in the range of $c_p \propto x^{-0.5}$ to $c_p \propto x^{-2.5}$.

2.5.2.4. Overblowing

Stopped pipes also tolerate a wider range of jet velocities in the first oscillating regime, compared to open pipes. Experimental observations in open pipes show that for a Reynolds number as high as 5200, the Strouhal number $St_w = fW/u_0$ is expected to reach the

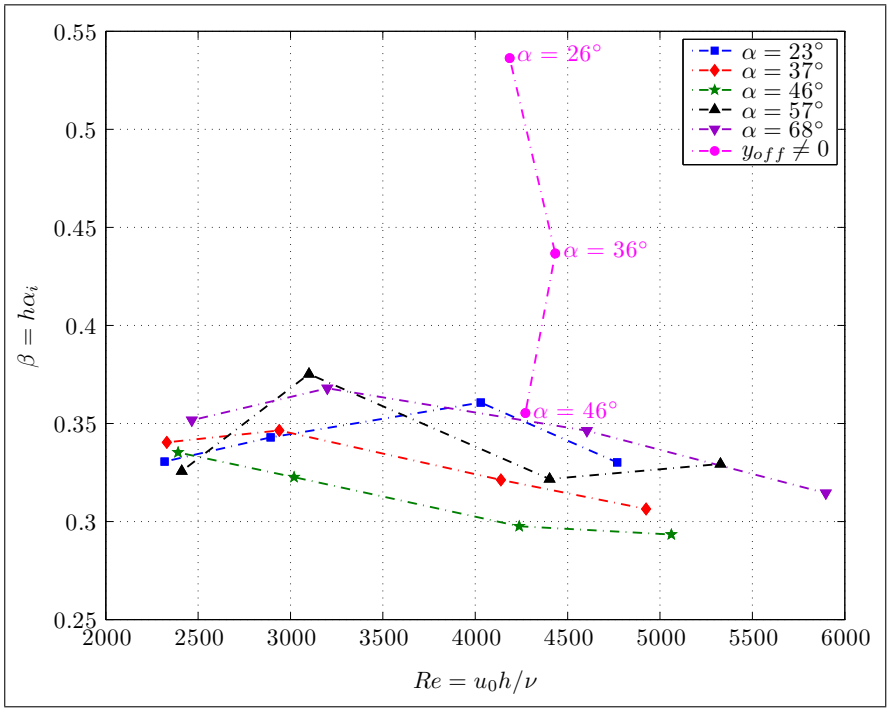

FIGURE 2.14. Growth factor $\beta = h\alpha_i$ versus the Reynolds number $Re = u_0 h/\nu$ for all the blowing conditions. If not specified in the legend, the offset y_{off} is null.

overblowing threshold of 0.07. The data collected in the present experiment (Figure 2.13 (lower graph)), shows that for $Re \sim 5200$ the lowest value of St_w observed is close to 0.1.

A second Strouhal number St^* (see Eq. 2.12) that accounts for the jet slowing is also displayed in Figure 2.13. Although it shows the same behavior as St_w, the values of St^* are greater due to a corrected jet velocity, and may be a more accurate measure of the system's ability to overblow. A thorough analysis of this phenomenon demands the careful consideration of the evolution of the central velocity of the jet. As the initial velocity u_0 is raised, turbulent mixing on the jet is triggered closer to the flue and thus the characteristic slowing caused by turbulence has a greater impact. As a consequence, a higher velocity is necessary to achieve the overblowing, which has the musical advantage of allowing a larger dynamic range within the first register. Along with the hydrodynamical consideration, increasing the jet velocity also affects the oscillating frequency, which, in the present experiment, can be increased by as much of one quarter tone.

2.5.3. Acoustical Analysis

Characteristic spectra of the closed end oscillating pressure p' are plotted in Figure 2.15 for two different configurations. The spectra show harmonics as well as a strong broadband noise filtered by the resonator. An unexpected antiresonance modulates the broadband noise around 1600 Hz, which is probably a consequence of the visualization window. The broadband noise highlights the response of the resonator and thus the pipe modes become visible in the spectrum. The frequency ratio of the pipe modes follows an approximate relation of odd integers of the fundamental, but toward the higher modes this relation becomes more inharmonic and also depends on the orientation angle of the jet, α.

Over all the blowing conditions, the fundamental frequency varies around the resonance frequency $f_1 = 686$ Hz (see Figure 2.16, top), showing a maximum deviation of $\pm 3\%$ (a quarter tone) for the two extreme conditions (-3 % for (Re=2400,α=24°) and +3 % for (Re=5200,α=69°)). The fundamental frequency increases with the Reynolds number and with the aperture of the open end (as the angle α increases).

The spectral content is characterized by the harmonics, odd and even, and the broadband noise. The amplitude of the harmonics is estimated by computing a discrete Fourier transform (DFT) over a window that includes an integer number of oscillation periods (30 periods with a sample rate of 25 kHz). Therefore, the amplitude of each bin of the DFT includes the energy within a band of 22.5 Hz. The broadband noise is estimated by averaging a DFT computed over a much larger window (3000 periods). Harmonics and noise estimation are displayed in Figure 2.16 (bottom).

The amplitude of the fundamental is always larger by at least 30 dB than the one of the third (and other) harmonics. The whole spectral content follows the same trend as the fundamental for all the blowing conditions: the amplitude increases with the Reynolds number. The first and third harmonics are higher than the second, which has almost the same level as the noise. When the jet is aimed at the center of the bore (Figure 2.15, gray, top), the energy balance between odd and even harmonics is modified: the amplitude of the second harmonic exceeds that of the third. However, even harmonics are radiated less

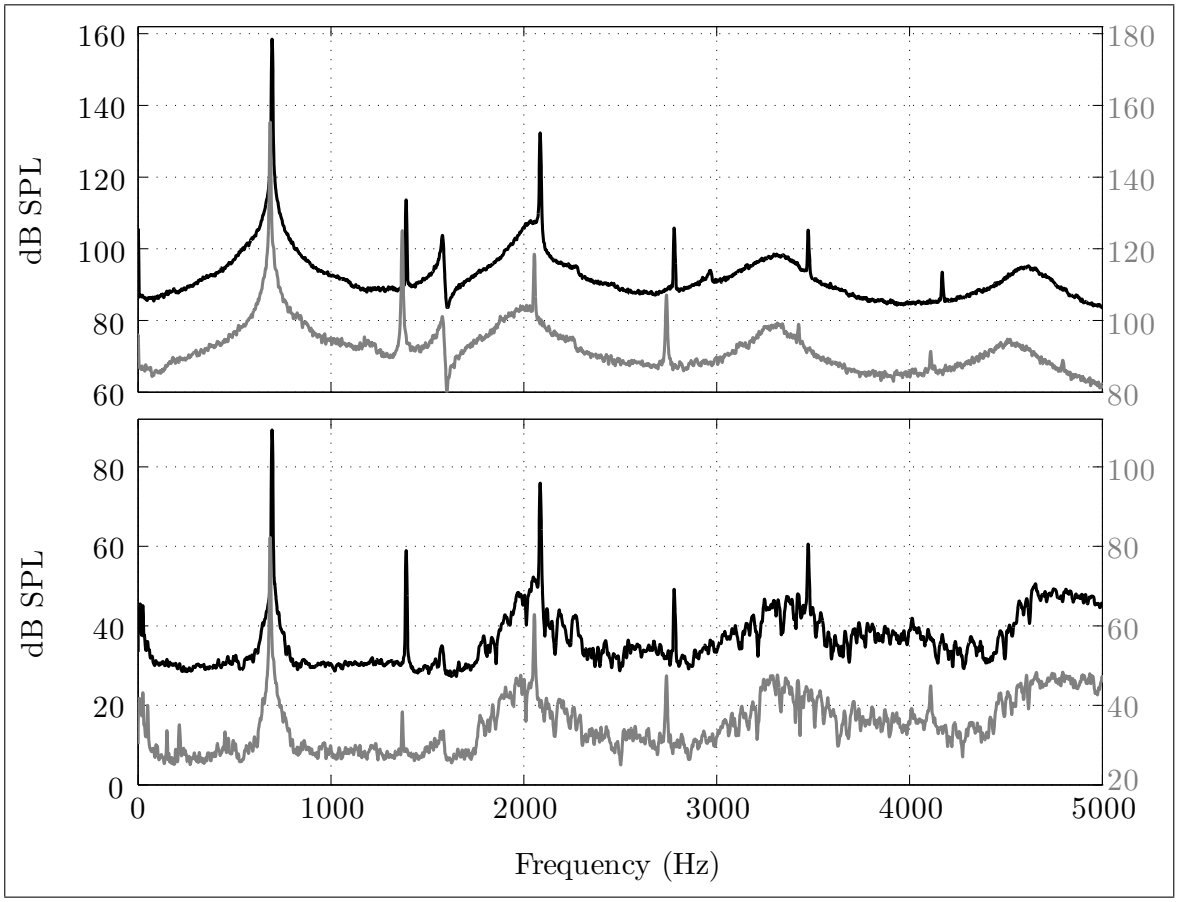

FIGURE 2.15. Spectra of the oscillating part of the pressure at the closed end (top) and of the radiated sound (bottom) for two runs of the experiments: blowing condition $Re = 5200$, $\alpha = 24°$, $y_{\text{off}} = 0$ mm (black) or 3 mm (gray, shifted by -20 dB). The spectra are estimated through a power spectral density using a 8192 points DFT averaged over ∼30 windows of length 0.33 s.

effectively than odd ones: for the case $y_{\text{off}} = 3$ mm (Figure 2.15, gray, bottom), the second harmonic of the radiated sound is lower than the third one whereas this is reversed for the internal pressure signal.

The amplitude of oscillation of the pressure at the closed end p' makes it possible to estimate the ratio of the acoustic velocity over the jet velocity through the dimensionless amplitude proposed by Verge *et al.* (Verge, Fabre, & Wijnands, 1997) $p'_1/\rho c_0 u_0$, where p'_1 is the amplitude of the fundamental. The dimensionless amplitude is displayed in Figure 2.17. It slightly increases with the Reynolds number but remains under the usual value, ∼0.2,

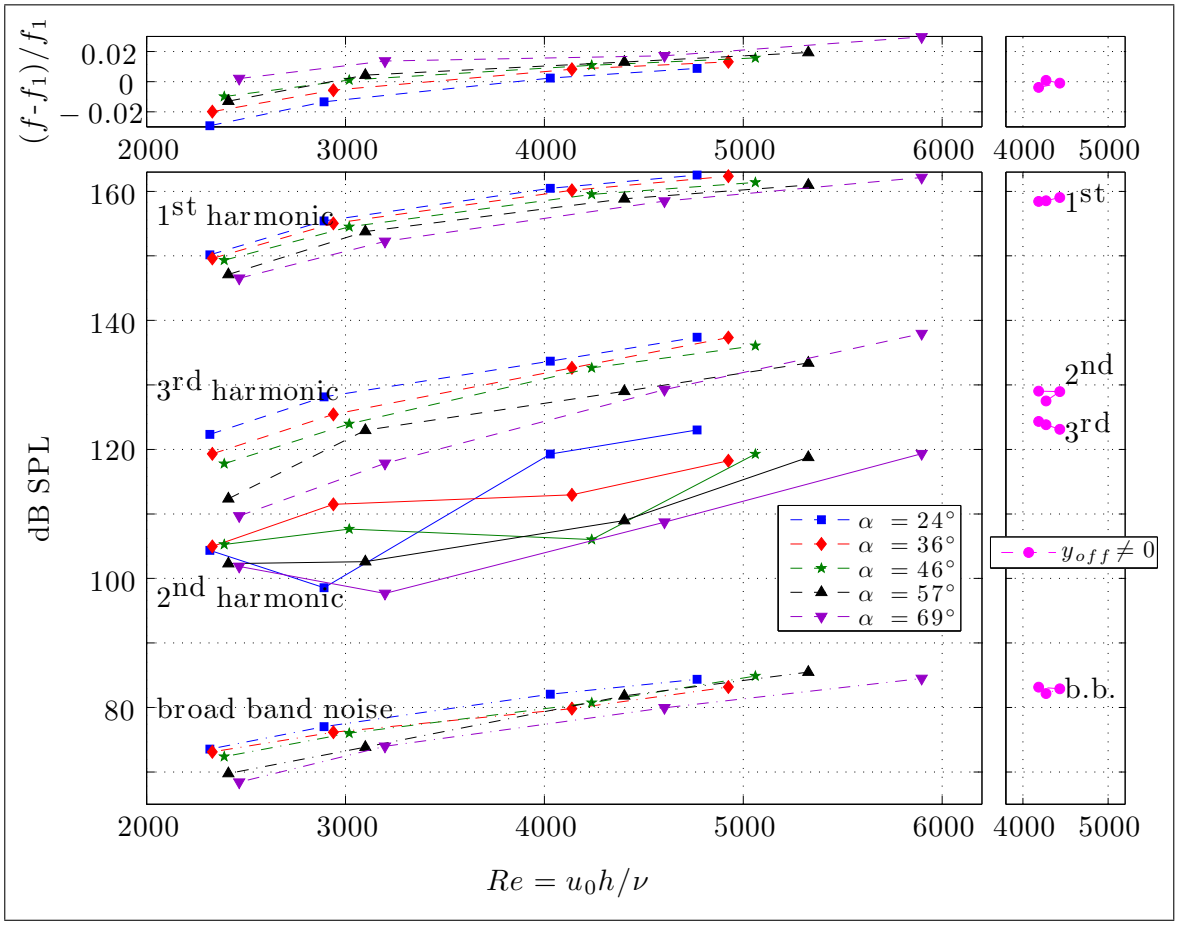

FIGURE 2.16. Deviation in the fundamental frequency $(f - f_1)/f_1$ with $f_1 = 686$ Hz (top) and harmonics and broadband noise levels of the internal pressure p' (bottom) versus the Reynolds number $Re = u_0 h/W$ (dashed lines: first and third harmonics; solid lines: second harmonics; dash-dot lines: broadband noise). If not specified in the legend, the offset y_{off} is null. For the case $y_{\text{off}} \neq 0$, the second harmonics are higher than the third ones.

found by other authors for different types of flutes and blowing conditions. Additionally, a clear consequence of the variation of the angle α is observed: for a jet directed towards the labium, the amplitude of oscillation increases about 5 dB as the angle decreases from 69° to 24° (the jet aligns with the pipe axis).

2.6. Conclusions

Some fundamental aspects of the hydrodynamics of stopped end pipes have been discussed analytically and observed in a controlled experiment. The musician has direct control over several parameters, such as the jet-labium offset y_{off}, the central velocity of the jet u_0, and the jet-pipe angle α. Changes in any of these three parameters have an incidence on the hydrodynamic behavior and thereby on the acoustic behavior. We have observed that a wide range of these parameters produces sound.

The turbulent jet instability was measured observing that the growth rate for a transversal perturbation is of the same order of magnitude as for a laminar jet ($\beta = h\alpha_i \simeq 0.24$). The amplification coefficient α_i is larger when the jet is directed to the center of the bore ($\beta = h\alpha_i \sim$ 0.25 to 0.38), also displaying a dependence on the jet-pipe angle α. The increase of β and the subsequent saturation of the source mechanisms may have an impact on the spectral content and on the triggering of nonlinear mechanisms such as the vortex shedding (B. Fabre and & Wijnands, 1996). The jet's central velocity is constant in the laminar jet core but decreases according to $u_0 \propto x^{-1/2}$ and also spreads linearly with x in the fully developed turbulent region (Thwaites & Fletcher, 1980). The velocity of convection of the perturbation (c_p), which depends on the jet's central velocity, is affected by the regime transition and shows an x-dependence similar to the one expected for the centerline velocity u_0.

A remarkable observation has to do with the auto-direction of the jet toward the labium in stopped pipes. The player does not need to aim the jet directly at the labium in order to produce a stable oscillation. This behavior has already been formulated theoretically (Fletcher, 2005) and is now measured experimentally. The mean deflection of the jet centerline due to air recirculation within the pipe seems to act only on the first half of the jet. When the jet is directed to the labium, the resulting deflection at the labium is small compared with the open-open pipe case. But when the jet is not directed at the labium but towards the center of the pipe inlet, the mean deflection makes the jet bend back toward the labium, providing a total deflection that is, on average, three times higher than that of the

former case. The mean jet centerline position is almost entirely fixed by the aerodynamic balance rather than by the lip's configuration, as it would be in the case of an open-open pipe.

The effect of the crossflow was successfully modeled as a deviation of the jet's centerline with a polynomial dependence on the horizontal distance $\langle\eta\rangle/rh = a(x/rh)^{\delta}$, with $\delta \simeq 2$. The model proved to be valid for the first half of the jet length. The magnitude of this deviation depends strongly on the jet–labium offset.

Any change in the symmetrical properties of the non-linear exciter is known to affect the relative strength of the harmonics. This is the case of the offset between the jet axis and the labium (Fletcher & Douglas, 1980). Although in stopped pipes part of this offset is corrected by the steady deflection, the equilibrium point of the oscillating jet is still slightly shifted above the labium, producing an asymmetrical jet impact. Consequently, the amplitude of the second harmonic has been found to be greater for larger values of the initial jet-labium offset. The deflection mechanism makes it possible to produce stable oscillations for a large range of jet offsets, while maintaining the ability to control the harmonic generation as it can be performed on a lip–blown open–open pipe, such as the transverse flute.

Another striking point is the wide range of angles at which the pipe is able to produce stable oscillations. Both the oscillating frequency and the acoustic power are correlated with the angle: a shift in the frequency of -3% has been observed for a decrease of the angle (jet and pipe axis aligned) together with a variation in the amplitude of oscillation of about +5 dB. Moreover, the estimation of the ratio of the acoustic velocity over the jet velocity suggests that a damping mechanism holds the amplitude of oscillation below a critical value. The acoustic flow separation, which is known to be for the recorder and the flute a significant limiting factor in the growth of the amplitude of oscillation (B. Fabre and & Wijnands, 1996), might well be that damping mechanism, even if the constriction of the open end is not as important in the siku as in other flute-like instruments. The transfer of

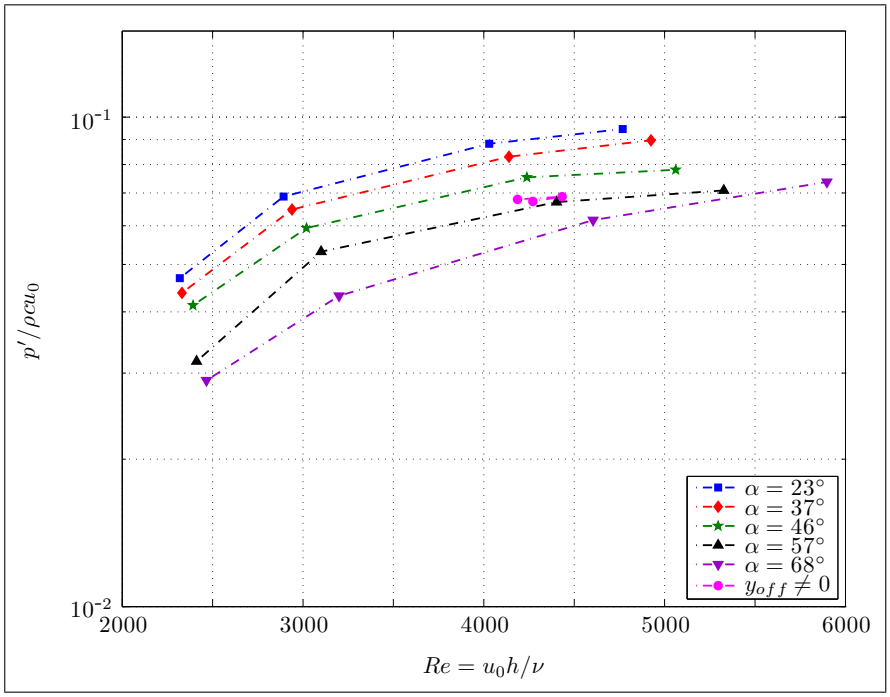

FIGURE 2.17. Dimensionless amplitude of oscillation $p'/\rho_0 c_0 u_0$ versus the Reynolds number $R = u_0 h/W$. If not specified in the legend, the offset y_{off} is null.

the energy towards the broadband noise due to turbulence also reduces the efficiency of the auto-oscillation process.

Therefore, from the standpoint of the musician, the production of a tone in a stopped pipe seems easier than in the case of an open-open flue instrument. This might partly explain why stopped pipes were the most common type of resonator found in ancient civilizations in the region.

References

Auvray, R., Fabre, B., & Lagree, P.-Y. (2012). Regime change and oscillation thresholds in recorder-like instruments. *Journal of the Acoustical Society of America*, *v. 131*(n. 2), 1574–1558.

Baines, A. (1967). *Woodwind instruments and their history*. London: Faber and Faber.

B. Fabre and, A. H., & Wijnands, A. P. J. (1996). Vortex shedding in steady oscillation of a flue organ pipe. *Acta Acustica United with Acustica*, *v. 82*, 863–877.

Blanc, F., de la Cuadra, P., Fabre, B., Castillo, G., & Vergez, C. (2010). Acoustics of the flautas de chino. *Proceedings of 20th International Symposium on Music Acoustics*.

Cambonie, T., Gautier, N., & Aider, J.-L. (2013). Experimental study of counter-rotating vortex pair trajectories induced by a round jet in cross-flow at low velocity ratios. *Experiments in Fluids*, *v. 54*, 1–13.

Coltman, J. W. (1967). Jet drive mechanism in edge tones and organ pipes. *Journal of the Acoustical Society of America*, *v. 60*, 725–733.

Coltman, J. W. (1968). Sounding mechanism of the flute and organ pipe. *Journal of the Acoustical Society of America*, *v. 4*, 983–992.

Cremer, L., & Ising, H. (1967-68). Die selbserregten schwingungen von orgelpfeifen. *Journal of the Acoustical Society of America*, *v. 19*, 143–153.

Crighton, D. G., & Gaster, M. (1976). Stability of slowly diverging jet flow. *Journal of Fluid Mechanics*, *v. 77*, 379–413.

de Arce, J. P. (1998). Sonido rajado: The sacred sound of chilean pifilca flutes. *The Galpin Society Journal*, *v. 51*, 17–50.

de Arce, J. P. (2002). Pre-colombian flute tuning in the southern andes. *Orient Archaologie*, *v. 10*, 291–310.

de la Cuadra, P. (2005). *The sound of oscillating jets: Physics, modeling and simulation in flute-like instruments* (Unpublished doctoral dissertation). Stanford University.

de la Cuadra, P., Smyth, T., Chafe, C., & Boaqiang, H. (2001). Waveguide simulation of neolithic chinese flutes. *Proceedings of ISMA, Internation Symposium on Musical Acoustics, Perugia, Italy*.

de la Cuadra, P., Vergez, C., & Fabre, B. (2007). Visualization and analysis of jet oscillation under transverse acoustic perturbation. *Journal of Flow Visualization and Image Processing*, *v. 14*, 355–374.

Elder, S. A. (1973). On the mechanism of sound production in organ pipes. *Journal of the Acoustical Society of America*, *v. 54*, 1553–1564.

Fabre, B., Gilbert, J., Hirshberg, A., & Pelorson, X. (2012). Aeroacoustics of musical instruments. *Ann. Review of Fluid Mech.*, *v. 44*, 1–25.

Fabre, B., & Hirschberg, A. (2012). Physical modeling of flue instruments: a review of lumped models. *Acta Acustica united with Acustica*, *v. 86*, 599–610.

Fletcher, N. H. (1976). Sound production by organ flue pipes. *Journal of Acoustic Society of America*, *v. 60*, 926–936.

Fletcher, N. H. (2005). Stopped-pipe wind instruments: Acoustic of the panpipes. *Journal of the Acoustical Society of America*, *v. 117*(n. 1), 370–374.

Fletcher, N. H., & Douglas, L. (1980). Harmonic generation in organ pipes, recorders, and flutes. *Journal of the Acoustical Society of America*, *v. 68*, 767–771.

Helmholtz, H. (1885). *On the sensation of tone* (8th ed. ed.). New York: Dover Edition.

Holger, D. K., Wilson, T. A., & Beavers, G. S. (1977). Fluid mechanics of the edgetone. *Journal of the Acoustical Society of America*, *v. 62*(5), 1116–1128.

Lin, J.-C., & Rockwell, D. (2001). Oscillations of turbulent jet incident upon an edge. *Journal of Fluids and Structures*, *v. 15*, 791–829.

Maes, F., Collingnon, A., Vandermeulen, D., & G. Marcha, P. S. (1997). Multimodality image registration by maximization of mutual information. *Medical Imaging, IEEE Transactions on*, *v. 16*, 187–198.

Mattingly, G. E., & Criminale, W. O. (1971). Disturbance characteristics in a plane jet. *Physics of Fluid*, *v. 14*, 2258–2264.

Muppidi, S., & Mahesh, K. (2005). Study of trajectories of jets in crossflow using direct numerical simulations. *Journal of Fluid Mechanics*, *v. 530*, 81–100.

New, T. H., Lim, T. T., & Luo, S. C. (2003). Elliptic jets in cross-flow. *Journal of Fluid Mechanics*, *v. 494*, 119–140.

New, T. H., Lim, T. T., & Luo, S. C. (2006). Effects of jet velocity profiles on a round jet in cross-flow. *Experiments in Fluids*, *v. 40*, 859–875.

Nolle, A. W. (1998). Sinuous instability of a planar air jet: Propagation parameters and acoustic excitation. *Journal of the Acoustical Society of America*, *v. 103*(n. 6), 3690–3705.

Plesniak, M. W., & Cusano, D. M. (2005). Scalar mixing in a confined rectangular jet in crossflow. *Journal of Fluid Mechanics*, *v. 524*, 1–45.

Powell, A. (1961). On the edge tone. *Journal of the Acoustical Society of America*, *v. 33*, 395–409.

Rayleigh, J. W. S. (1894). *Theory of sound* (2nd ed. ed.). New York: Dover Edition.

Schlichting, H., & Gersten, K. (2004). *Boundary layer theory* (8th ed. ed.). Berlin: Springer-Verlag.

Smith, S. H., & Mungal, M. G. (1998). Mixing, structure and scaling of the jet in crossflow. *Journal of Fluid Mechanics*, *v. 357*, 83-122.

Thwaites, S., & Fletcher, N. H. (1980). Wave propagation on turbulent jets. *Acustica*, *v. 45*, 175–179.

Thwaites, S., & Fletcher, N. H. (1982). Wave propagation on turbulent jets: Ii. growth. *Acustica*, *v. 51*, 44–49.

Tritton, D. J. (1988). *Physical fluid dynamics* (2nd ed. ed.). Oxford: Oxford University Press.

Verge, M. P. (1995). *Aeroacoustics of confined jets, with application to the physical modeling of recorder-like instruments.* (Unpublished doctoral dissertation). Eindhoven University of Technology.

Verge, M.-P., Fabre, B., Mahu, W. E. A., Hirschberg, A., van Hassel, R. R., Wijnands, A. P. J., . . . Hogendoorn, C. J. (1994). Jet formation and jet velocity fluctuations in a flue organ pipe. *Journal of Acoustic Society of America*, *v. 95*, 1119–1132.

Verge, M.-P., Fabre, B., & Wijnands, A. P. J. (1997). Sound production in recorder-like instruments . i. dimensionless amplitude of the internal acoustic field. *Journal of Acoustic Society of America*, *v. 101*, 2914–2924.

Verge, M.-P., Hirschberg, A., & R.Caussé. (1997). Sound production in recorderlike instruments . ii . a simulation model. *Journal of Acoustic Society of America*, *v. 101*, 2925–2939.

Wright, H. A. K., & Campbell, D. M. (1998). Analysis of the sound of chilean pifilca flutes. *The Galpin Society Journal*, *v. 51*, 51–63.

Yoshikawa, S. (1998). Jet wave amplification in organ pipes. *Journal of the Acoustical Society of America*, *v. 103*.

APPENDIX A. EXPERIMENTAL PROCEDURE

The fundamental aspects of the experimental design were laid out in section 2.3. Further details on equipment and the experimental protocols are presented in this appendix.

Schlieren photography allows for the visualization of the CO_2 jet, which is invisible to the human eye. Local variations in the refractive index (due to changes in the mass density) are turned into variations of the grayscale image. These density gradients are measured along a direction that can be controlled with the position of the edge of a knife placed just before the camera. Specific details on the implementation of a Schlieren setup can be found in various publications of authors that have followed this approach (Verge, 1995; de la Cuadra, 2005; de la Cuadra et al., 2007).

Figure A.1 shows the experimental array of the Schlieren system. The punctual light source that illuminates the jet is generated with the Oriel Xenon Flashlamp, and then filtered using a metal screen with a small aperture in the center. The flashlamp is controlled with the waveform generator TGA1244 from TTI, that emits pulses at a frequency of 8Hz. The digital camera 12-bit Cooled Imaging CCD by Sensicam is also controlled by the impulse signal, ensuring the synchronization between the illumination of the fluid and the acquisition of images.

Pressure signals are measured inside the control cavity, at the stopped end of the experimental pipe (internal acoustic field), and 29 cm away from the labium of the pipe (radiated acoustic field). The first two signals are conditioned using the Endevco 136 DC Differential Voltage Amplifier and third one with the Brüel & Kajaer Nexus Conditioning Amplifier. All three signals are then recorded with the National Instrumets SCB-68 Acquisition Board, connected to a Windows based machine. The impulse signal used to control the camera and the light source is recorded with the same board, after being conditioned and converted to square pulses with the ATO F77 Interstate 20MHz LOG-LINEAR Sweep Generator.

The CO_2 jet is controlled using a Brooks 5851S Smart Mass Flow. A complementary software provides access to the PID controller's parameters in order to adjust the response of the output signal, whose set point is defined in liters per minute.

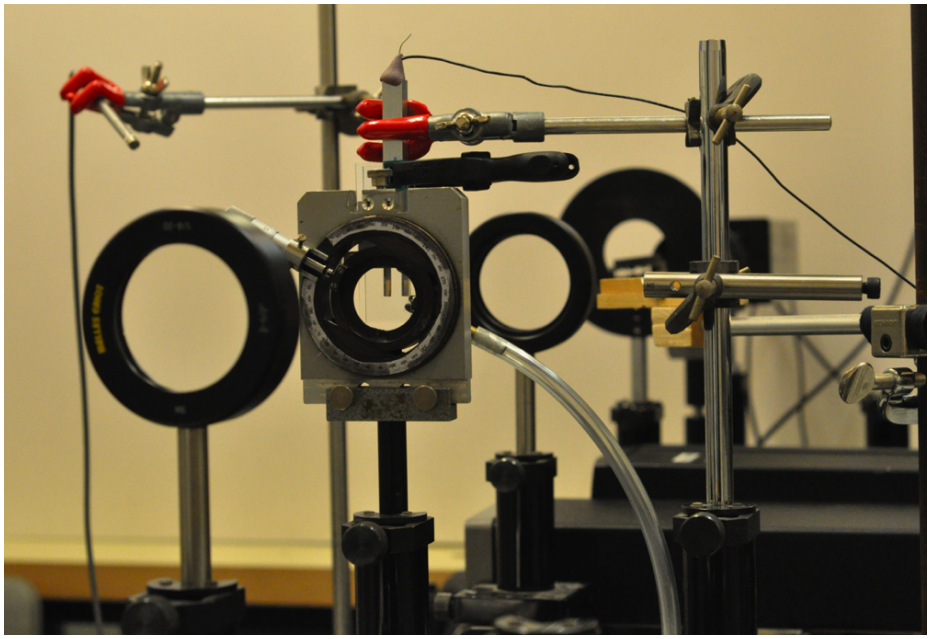

FIGURE A.1. Experimental setup of the Schlieren system. The black circles are, in ascending order of depth: 1) first glass of the Schlieren system, 2) optical device used to vary the jet angle α, 3) second glass of the Schlieren system, and 4) aperture of the visual field of the camera. The side of the camera is shown at the end of the path.

Synchronization of the analog signals and the images is achieved by introducing a stimulus that is common to both media. As it is common practice in film making, a sync slate produces a clap that can be heard by the radiated pressure sensor, and also visually captured by the camera. Figure A.2 displays the change of state of the sync slate: before and after the clap is produced. The camera pulse that comes immediately after the slate clap is synchronized with the first image that shows the slate shut. A simple script is then used to ensure that the amount of images in a run matches the amount of control square pulses, and also to link to each image to a sample of the analog signals.

The protocol used in each measurement was the following:

(i) Start the capture of analog signals

(ii) Adjust the set-point of the CO_2 flow controller and wait for the stabilization of the output pressure

(iii) Start the image acquisition loop

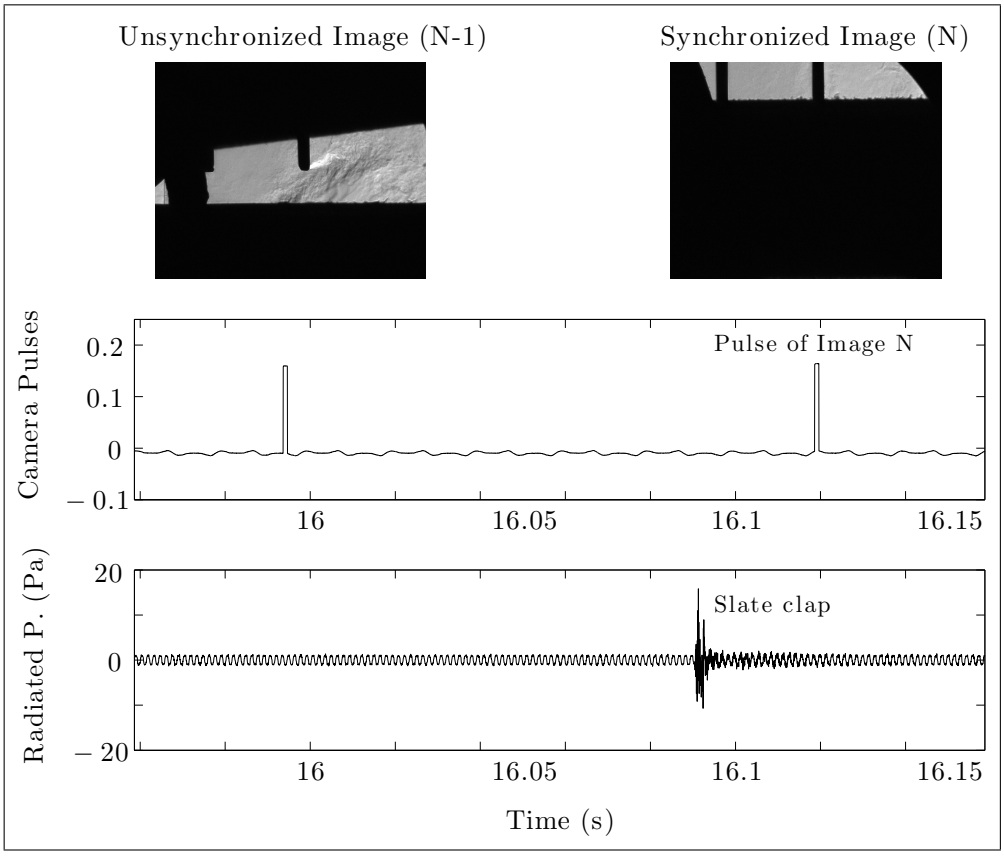

FIGURE A.2. Image and signals synchronization using a sync slate. The camera pulse that comes immediately after the slate clap is synchronized with the first image that shows the slate shut.

(iv) Produce a clap with the sync slate and then remove it from the visual path

(v) Wait until the image acquisition cycle is near to the end (∼45 seconds)

(vi) Reintroduce the sync slate in the visual path and produce a second clap

(vii) Change the flow controller set-point to zero

(viii) Stop the capture of analog signals

APPENDIX B. SELECTION OF A WINDOW OF ANALYSIS

A window of analysis S_W has to be selected, that is invariant between experiments and matches the axes definition of the model (see figure 2.3). As it is customary in the literature, the x-axis is defined as the initial streamwise direction of the jet. The former cannot be easily deduced from the images: the structure of the nozzle is irregular and the jet contains information of the oscillations and the mean deflection. The horizontal projection of the distance from the flue exit –the origin of the oscillations– up to the labium is W, and the orthogonal distance from the labium to the x-axis is the vertical misalignment y_{off}. In this experiments the jet has an inclination α relative to the main axis of the pipe. Figure B.1 illustrates this description.

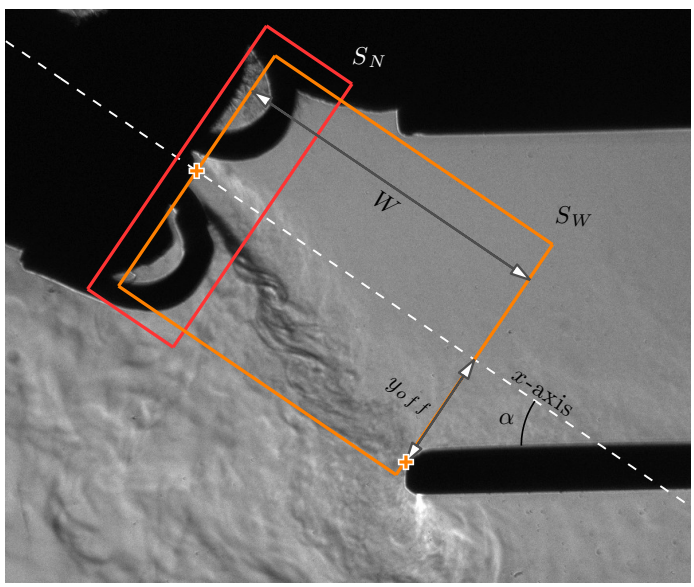

FIGURE B.1. Typical image with highlighted attributes of interest.

The total average of the array $\tilde{J}$ of aggregated images is calculated, which is expected to provide a better idea of the initial orientation of the jet. Thereafter, a straight line is manually adjusted to fit the direction of the first stages of the average jet, and the origin is placed at a point where the structure of the nozzle seems to end. This last definition is based solely on graphic considerations and may not coincide with the actual origin of the oscillations. Finally, a representative point at the edge of the labium is manually selected.

The definition of S_W has to be consistent for different geometrical configurations. The structure of the nozzle is an invariant marker and thus is used to link the window S_W across experiments. The image registration algorithm proposed in (Maes et al., 1997) was used to align the nozzle of two images. One is set as a reference, and the other is rotated and translated exhaustively in order to find an optimal pair of windows S_N that maximize the mutual information. Therefore, the window S_W is carefully defined for only one experiment, and the result is extrapolated to the rest by means of the alignment algorithm.

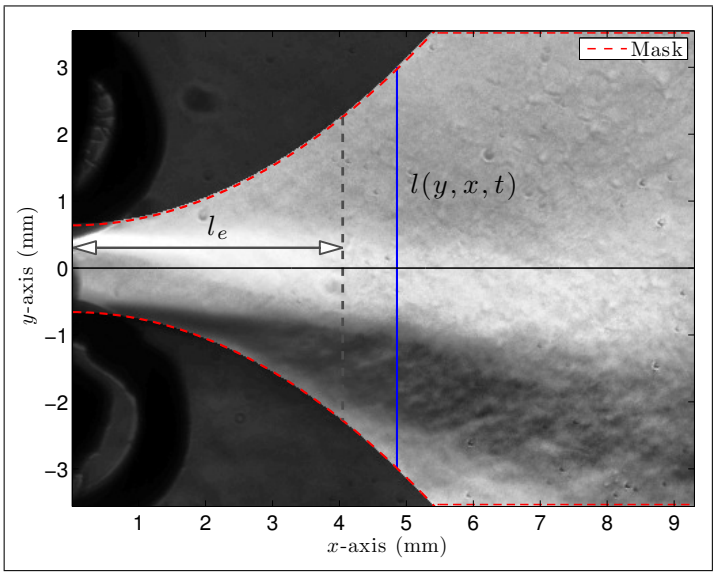

FIGURE B.2. Left: Analysis window S_W with quadratic mask used for the center-line detection.

A typical window of analysis is shown in figure B.2. The amplitude of the oscillations and the width of the jet are both larger as the distance x increases. In order to improve the resolution of detection, a quadratic mask (red dotted line in figure B.2) is used to select proportionally shorter gray profiles $l(y, x, t)$ near the flue.

APPENDIX C. VALIDATION OF THE JET DETECTION ALGORITHMS USING SYNTHETIC IMAGES

Synthetic images are created for the purpose of testing, under controlled conditions, the performance of the jet detection algorithms. The parameters used to simulate a complete cycle of oscillation of the jet wave are similar as those of the experimental jet. The initial width of the jet is $h = 0.7$ mm and the shear layers spread with an angle of 22°, yielding a final jet width similar to the experimental case. The wavy perturbation of Equation C.1 is used to displace the jet over a range of $x = [0, 12]$ mm:

$$\eta'(x,t) = \eta_0 e^{\alpha_i x} e^{i\omega(t - x/c_p)}, \tag{C.1}$$

where the parameters are $\eta_0 = 0.05$, $\alpha_i = 0.33$, $c_p = 10$ m/s, and $f = \omega/2\pi = 670$ Hz. The result is an image like that of in Figure C.1.

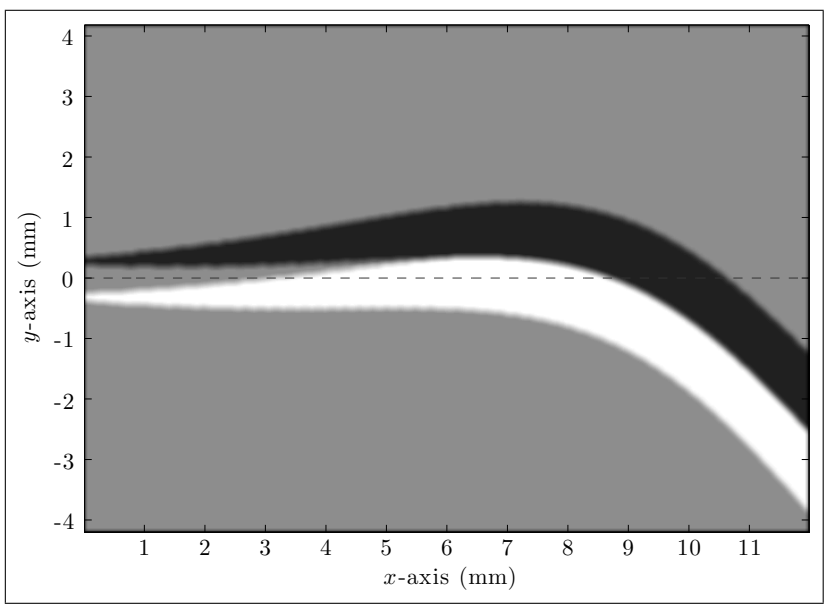

FIGURE C.1. Synthetic image of the jet using the wavy perturbation of Equation C.1 with parameters: $\alpha_i = 0.33$, $\eta_0 = 0.05$, $c_p = 10$ m/s, and $f = \omega/2\pi = 670$ Hz.

In order to simulate the effects of small scale vortical structures of the turbulent jet, consecutive rounds of noise are added to the images. Gaussian noise of mean 0 and variance of 50% is used for this purpose. A level of Noise=2 means applying Gaussian noise two

consecutive times, and so on. After the corresponding layers of noise, a Gaussian filter with a squared mask of 8 pixels wide and a standard deviation of 4 pixels is applied to the whole image, with the aim of reducing the spatial frequency of noise.

Finally, a reconstruction of a complete cycle of oscillation in 300 synthetic images is used to test the aggregation process, the jet detection, and the curve fitting of the parameters of the aeroacoustic models.

C.1. Image Aggregation

The parameters of the image aggregation algorithm are the spread parameter ζ and the number of images M. Only the former is relevant for the validation process, and the second is set at $M = 32$ as with the experimental data. Figure C.2 shows the result of applying the image aggregation algorithm to clean images and images with levels of noise 3 and 4. Rows correspond to values of $\zeta = 0°$ (single-shot), 2°, 4.1°, 8.2°, and 16.4°.

The first column shows the effect of widening the parameter ζ: for large amplitudes of oscillation, the aggregation becomes destructive since images of distant phases are considered in the calculus. With $\zeta = 8.2°$, the centerline becomes blurry for $x > 8$mm, and the effect is even more pronounced for $\zeta = 16.4°$. However, for large levels of noise, a wider spread (ζ) is more effective at revealing the structure of the jet, even when it is almost impossible to differentiate it form the background noise in a single-shot image. Therefore, a reasonable compromise between a good tolerance to noise and an aggregation that does not corrupt the centerline is $\zeta \sim 8.2°$ (the value used in the experimental images is 8.4°).

C.2. Jet Detection

The detection of the jet centerline is now tested under different noise levels, on both single-shot and aggregated ($\zeta = 8.2°$) images. Figure C.3 summarizes this process.

As it was stated in the previous section, aggregated images tend to corrupt the centerline for large amplitudes of the vertical displacement. In the first row of Figure C.3, it is possible to observe that the jet detection performs better on single-shot images. However,

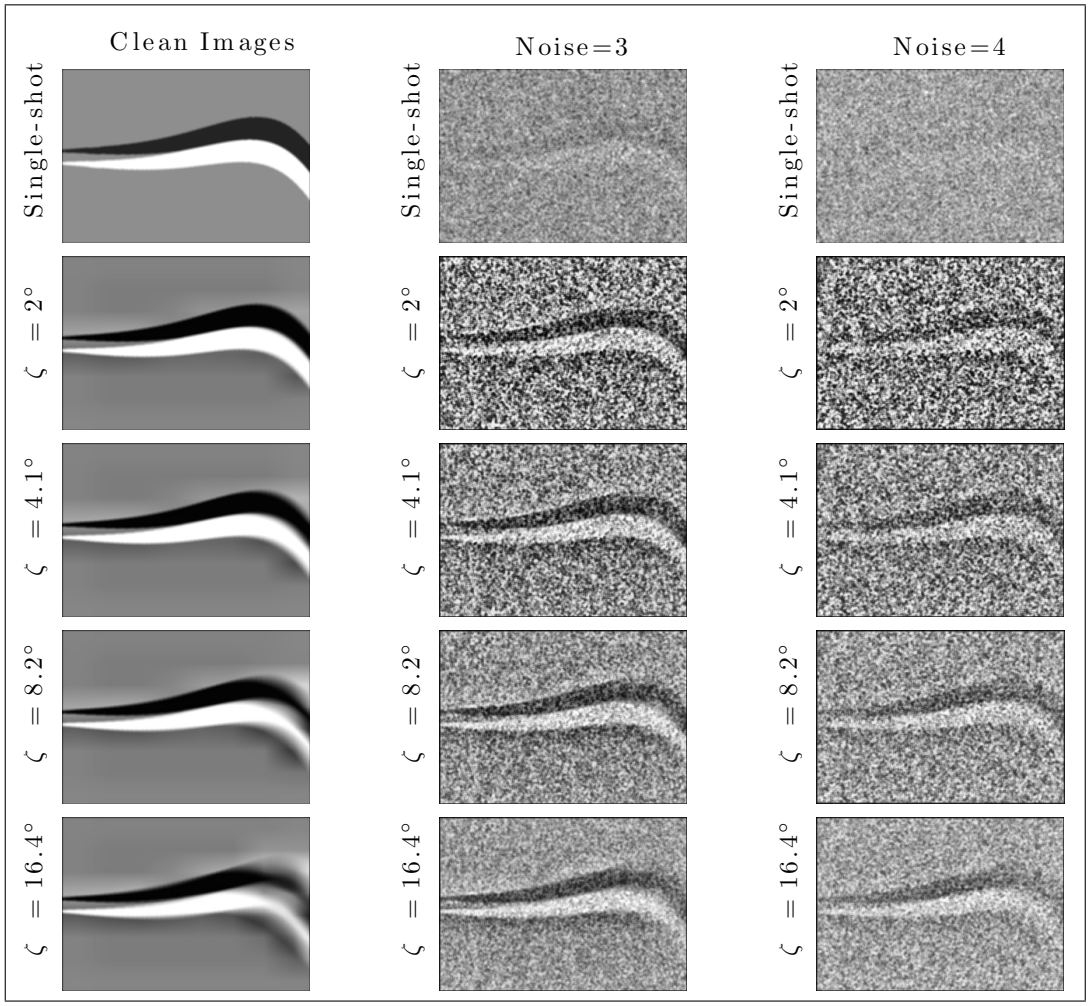

FIGURE C.2. Image aggregation results for different values of the spread parameter ζ, for Noise=0 (leftmost column), Noise=3 (center column) and Noise=4 (rightmost column).

for $x < 10$ mm, the differences are negligible. As the images become noisy, so does the detected centerline. The jet cannot be detected in single-shot images beyond Noise=2. In aggregated images, although the detection is noisy near the origin and the end for Noise$\leq$3, a reconstruction of the jet wave is possible even for Noise=4.

C.3. Instability Curve Fitting

The final figure of performance of the whole process is the estimation of the parameters of Equation C.1 by means of curve fitting. The amplitude of the detected jet wave $|\eta'|$

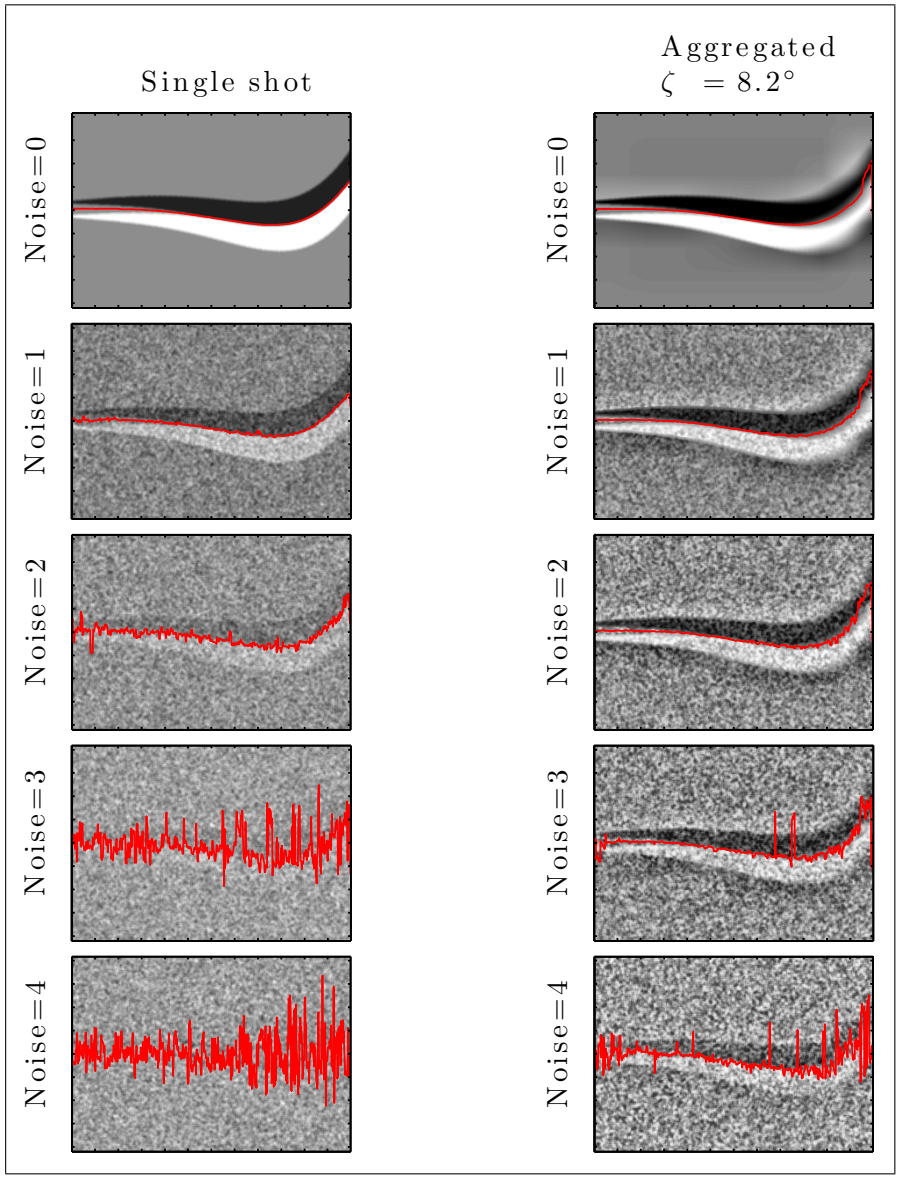

FIGURE C.3. Jet detection of single-shot (left column) and aggregated (right column) images using $\zeta = 8.2°$ for different configurations of noise.

is fitted with the curve $\eta_0 e^{\alpha_i x}$, and since the convection velocity was defined as linear $c_p \sim \frac{1}{2}x$, it is derived form the first order polynomial approximation of the phase $\phi_{\eta'}(x)$, using $c_p = \omega(d_x\phi_{\eta'})^{-1}$. Figure C.4 shows the curve fitting process for single-shot and aggregated images with Noise=2. In this visualization, the reduction of detection noise with aggregated images is evident, as well as the poor performance of the latter for large amplitudes of displacement ($x/h \simeq 15$ and onwards).

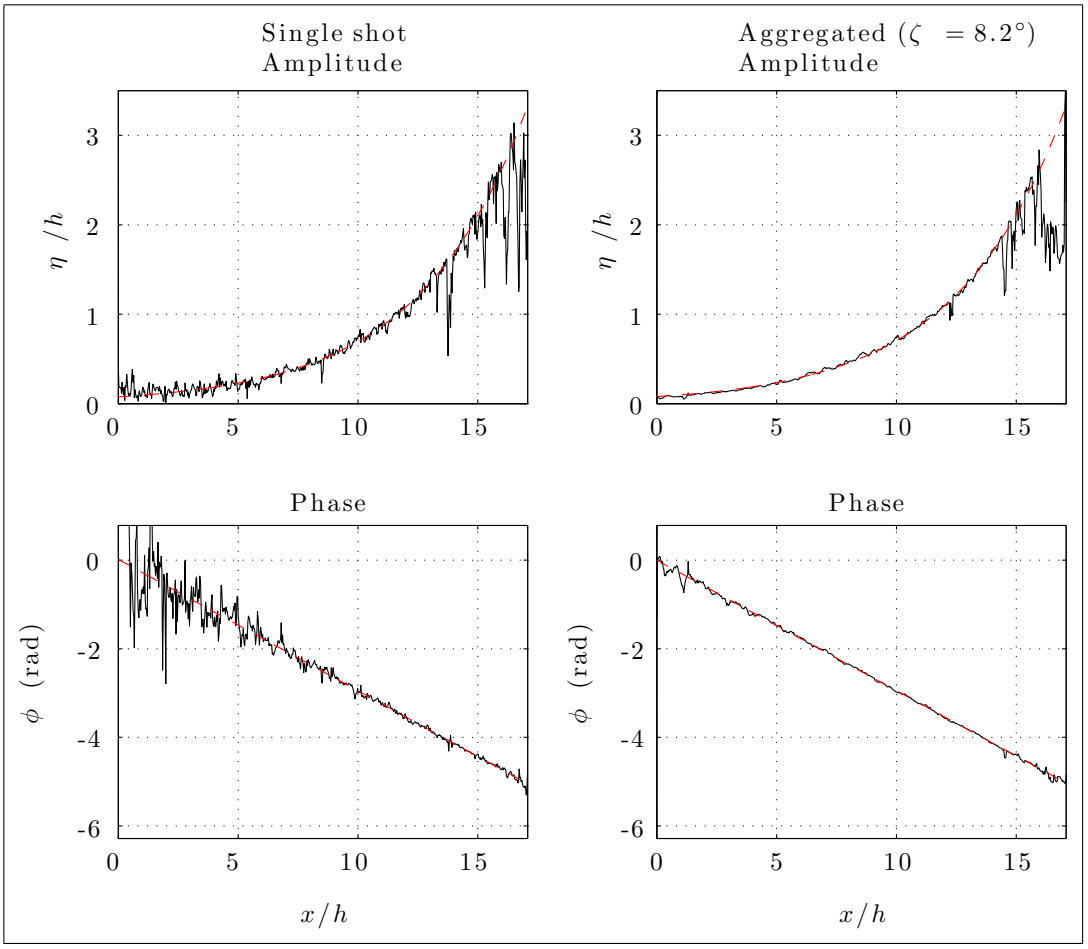

FIGURE C.4. Curve fitting of the amplitude and phase of the jet wave on synthetic images with Noise=2.